

DCReg: Decoupled Characterization for Efficient Degenerate LiDAR Registration

The International Journal of Robotics Research
00(0):1–24
©The Author(s) 2016
Reprints and permission:
sagepub.co.uk/journalsPermissions.nav
DOI: 10.1177/ToBeAssigned
www.sagepub.com/

SAGE

Xiangcheng Hu¹, Xieyuanli Chen², Mingkai Jia¹, Jin Wu³, Ping Tan¹, Steven L. Waslander⁴

Abstract

LiDAR point cloud registration is fundamental to robotic perception and navigation. However, in geometrically degenerate or narrow environments (e.g., corridors), registration problems become ill-conditioned, leading to unstable solutions and degraded accuracy. While existing approaches attempt to handle these issues, they fail to address the core challenge: accurately detection, interpret, and resolve this ill-conditioning, leading to missed detections or corrupted solutions. In this study, we introduce **DCReg** (*Decoupled Characterization for ill-conditioned Registration*), a principled framework that systematically addresses the ill-conditioned registration problems through three integrated innovations. **First**, DCReg achieves **reliable ill-conditioning detection** by employing a *Schur complement* decomposition to the hessian matrix. This technique decouples the registration problem into clean rotational and translational subspaces, eliminating coupling effects that mask degeneracy patterns in conventional analyses. **Second**, within these cleanly subspaces, we develop **quantitative characterization** techniques that establish explicit mappings between mathematical eigenspaces and physical motion directions, providing actionable insights about which specific motions lack constraints. **Finally**, leveraging this clean subspace, we design a **targeted mitigation** strategy: a novel preconditioner that selectively stabilizes only the identified ill-conditioned directions while preserving all well-constrained information in observable space. This enables efficient and robust optimization via the *Preconditioned Conjugate Gradient* method with a single physical interpretable parameter. Extensive experiments demonstrate DCReg achieves at least 20% - 50% improvement in localization accuracy and 5-100 times speedup over state-of-the-art methods across diverse environments. Our implementation will be available at <https://github.com/JokerJohn/DCReg>.

Keywords

LiDAR Degeneracy, Point Cloud Registration, Ill-conditioning, LiDAR SLAM

1 Introduction

1.1 Motivation and Challenges

LiDAR-based perception forms the foundation of modern autonomous systems, from self-driving vehicles to industrial robots. At its core, point cloud registration, enables these systems to build spatial understanding through applications in motion estimation Wu et al. (2022); Xue et al. (2025), mapping Ye et al. (2019); Qin et al. (2020); Shan et al. (2020); Hu et al. (2024a), localization Hu et al. (2024b), calibration Jiao et al. (2021b); Wu et al. (2019, 2021), and scene reconstruction Huang et al. (2021). Despite its fundamental importance, LiDAR registration remains inherently vulnerable to failure in geometrically degenerate environments such as corridors, tunnels, and open fields, where repetitive patterns or sparse features predominate. These challenging scenarios inherently lack sufficient geometric constraints along specific motion directions, resulting in rank-deficient or near-singular information matrices Nashed et al. (2021) that render the optimization problem ill-conditioned. This numerical ill-conditioning makes the solution highly sensitive to sensor noise and initial estimates, which manifests as amplified error propagation and unstable solutions, ultimately leading to catastrophic failures in autonomous navigation. Consequently, even minor perturbations in sensor measurements or initial estimates can

induce catastrophic divergence in the solution, precipitating complete navigation failure. The ability to understand and resolve such ill-conditioning is thus not merely a technical optimization but a prerequisite for deploying reliable autonomous systems for real-world applications.

Current approaches Tuna et al. (2023, 2025); Zhang et al. (2016) typically adopt a detect-then-mitigate paradigm, yet they fail to address the fundamental questions: when, why, and how does registration become ill-conditioned? This failure stems from three interconnected challenges:

- **When to detect:** Existing detection methods Hinduja et al. (2019); Hu et al. (2024b); Tuna et al. (2023); Zhang and Singh (2014) analyze the the

¹Department of Electronic and Computer Engineering, Hong Kong University of Science and Technology, Hong Kong, China

²Department of Mechanical Engineering at National University of Defense Technology, Changsha, Hunan

³School of Intelligent Science and Technology, University of Science and Technology Beijing, Beijing, China

⁴University of Toronto Institute for Aerospace Studies and the University of Toronto Robotics Institute, Toronto, Canada

Corresponding author:

Jin Wu, Full Professor, School of Intelligent Science and Technology, University of Science and Technology Beijing, Beijing, China

Email: wujin@ustb.edu.cn

Hessian spectral in optimization, where inherent scale disparity and coupling effects between translation and rotation mask critical ill-conditioning patterns. This coupling causes rotational degeneracy to be masked by translational eigenvalues, leading to missed detections or over-detections in precisely those scenarios where robots are most vulnerable.

- **Why it fails:** Even when ill-conditioning is detected, current methods [Hu et al. \(2024b\)](#); [Hinduja et al. \(2019\)](#) cannot explain which physical motions are degenerate and characterize to what extent they are degenerate. The mathematical abstractions (eigenvectors) remain ambiguous from the physical reality of robot motion, leaving practitioners without actionable insights for navigation decisions or system design improvements.
- **How to mitigate:** Existing mitigation strategies, whether regularization [Golub et al. \(1999\)](#); [Tuna et al. \(2025\)](#), truncation [Hansen \(1990\)](#), or remapping [Zhang and Singh \(2014\)](#); [Zhang et al. \(2016\)](#), apply blanket corrections that fundamentally alter the optimization problem. They either inject artificial constraints where none exist or discard valid information, inadvertently corrupting well-constrained directions while attempting to stabilize ill-conditioned ones.

These fundamental limitations motivate us to rethink ill-conditioned registration from first principles. Rather than treating it as an inevitable failure mode requiring external sensors or ad-hoc workarounds, we ask: can we develop a self-contained numerical framework that fundamentally understands and resolves ill-conditioning? Specifically, we seek an approach that: (i) reliably detects ill-conditioning by properly accounting for the inherent structure of the registration problem; (ii) provides quantitative, physically interpretable diagnosis of specific degenerate motions; and (iii) stabilizes the optimization without corrupting well-constrained directions. Our goal is a real-time solution that maintains mathematical integrity, ultimately enabling robust autonomous operation where current methods fail.

1.2 Contributions

This paper introduces a comprehensive framework to address ill-conditioned LiDAR registration problems.

Our first contribution ([Section 4](#)) is a scale-robust and coupling-aware formulation for ill-conditioning detection that addresses fundamental limitations of traditional eigenvalue-based frameworks. Due to inherent scale disparities between translation and rotation ([Section 3.3](#)) and environmental variations, we analyze eigen-spectral properties by separating translation and rotation subspaces ([Section 4.2](#)). This scale-consistent approach avoids both over- and under-detection without frequent parameter tuning ([Section 4.3](#)), unlike full Hessian analysis [Hinduja et al. \(2019\)](#); [Zhang and Singh \(2014\)](#); [Zhang et al. \(2016\)](#). Crucially, our novel approach employs the *Schur complement* to properly account for coupling effects between translation and rotation components ([Section 4.4](#)), enabling analysis within clean subspaces that exposes hidden degeneracies masked by conventional methods [Tuna et al. \(2023\)](#).

While detecting ill-conditioning in translation or rotation subspaces is necessary, such detection remains insufficient

for guiding practical applications without mapping to specific physical motion directions [Hu et al. \(2024b\)](#); [Zhang et al. \(2016\)](#). This challenge stems from inherent ambiguities in *Eigen Decomposition* (EVD) or *Singular Value Decomposition* (SVD), eigenvectors are typically arranged by ascending/descending eigenvalues without physical meaning. Additionally, when *eigenvalue clustering* occurs (near multiplicity), the eigen direction within degenerate subspaces become poorly constrained that lack consistent physical correspondence during iterations. To tackle this issue, **our second contribution** ([Section 5](#)) is a physically interpretable directional ill-conditioning analysis with quantitative characterization. We demonstrate how to: (i) identify specific ill-conditioned directions within subspaces via inner product analysis ([Section 5.1](#)), (ii) solve for the linear coefficients that combine ill-conditioned directions and physical motion axes ([Section 5.2](#)), and (iii) construct stable orthogonal bases aligned with parameter space using *Gram-Schmidt orthogonalization* to ensure interpretability despite eigenvector ambiguities ([Section 5.3](#)).

Our third contribution ([Section 6](#)) is a targeted ill-conditioning mitigation solver that transforms the original ill-conditioned problem into an equivalent but well-conditioned optimization while preserving all constraint information. Unlike Tikhonov regularization [Golub et al. \(1999\)](#); [Tuna et al. \(2025\)](#) or truncated SVD [Hansen \(1990\)](#) that indiscriminately modify the problem by either adding artificial constraints or discarding valid information, our approach maintains the integrity of the original problem ([Section 6.3](#)). Leveraging the aligned orthogonal bases and clean subspaces, we design a preconditioner that performs cluster-wise eigenvalue clamping, applying uniform spectral modification within each degenerate subspace to avoid numerical artifacts ([Section 6.2](#)). This enables targeted stabilization via *preconditioned conjugate gradient* ([Section 6.1](#)) with a single interpretable parameter controlling the condition number bound.

Our fourth contribution ([Section 7.5](#)) demonstrates the scalability and efficiency of our framework in real-world robotics applications. Our detection module can be seamlessly integrated with existing mitigation methods, significantly enhancing performance in degenerate registration scenarios ([Section 7.5.2](#)). Furthermore, benefiting from the convergence properties and the implementation of our methods, we achieve 5-100 times speedup compared to state-of-the-art approaches in long-duration experiments ([Section 7.3.2](#)).

2 Related Work

Addressing ill-conditioned registration typically involves two steps: detection and mitigation.

2.1 Ill-Conditioning Detection

Existing ill-conditioning detection methods can be categorized into spectral analysis and adaptive modeling approaches.

2.1.1 Spectral Analysis Methods Spectral analysis methods rely on analyzing information, covariance, or Hessian matrices from the optimization problem. [Zhang and Singh \(2014\)](#); [Zhang et al. \(2016\)](#) pioneered the use of minimal eigenvalues for ill-conditioning detection. However, this approach requires frequent parameter tuning across different

Table 1. Technical Characteristics of Degeneracy-Aware Registration Algorithms

Methods	Ill-conditioning Handling		Spectral Analysis		Parametrization	Space	Frame
	Detection	Mitigation	Scale	Coupling			
ME-SR Zhang and Singh (2014)	Eigenvalue	Projection	✗	✓	$\mathbb{R}^3 \times SO(3)$	Eigen	\mathcal{B}
ME-TSVD Tuna et al. (2025)	Eigenvalue	TSVD	✗	✓	$\mathbb{R}^3 \times SO(3)$	Eigen	\mathcal{B}
ME-TReg Tuna et al. (2025)	Eigenvalue	Regularization	✗	✓	$\mathbb{R}^3 \times SO(3)$	Eigen	\mathcal{B}
FCN-SR Hinduja et al. (2019)	Cond.	Projection	✗	✓	$\mathbb{R}^3 \times SO(3)$	Eigen	\mathcal{B}
SuperLoc Zhao et al. (2024b)	Statistics	✗	✗	✓	$\mathbb{R}^3 \times S^3$	Parameter	\mathcal{B}
X-ICP Tuna et al. (2023)	Sampling	Constrained	✓	✗	$\mathbb{R}^3 \times SO(3)$	Parameter	\mathcal{W}
DCReg (Ours)	Cond.	PCG	✓	✓	$\mathbb{R}^3 \times SO(3)$	Parameter	\mathcal{B}

Note: **Abbreviations:** Cond. = Condition number. Frame denotes the coordinate system for pose optimization. \mathcal{B}/\mathcal{W} = Body/World frame.

environments, as eigenvalues vary significantly with scene structure, initial pose, and measurement quantity. Alternative approaches utilize various quantitative metrics of covariance matrices, including determinants, traces, and D-optimality [Carrillo et al. \(2015\)](#); [Liu et al. \(2021\)](#); [Jiao et al. \(2021a\)](#); [Khattak et al. \(2020\)](#); [Zhao et al. \(2024b\)](#). Despite their theoretical foundation, these uncertainty-based metrics exhibit even greater sensitivity to environmental variations than minimum eigenvalue approaches, exacerbating the parameter tuning challenge. To address parameter sensitivity, [Nashed et al. \(2021\)](#) proposed using condition numbers of the full Hessian matrix, yielding more consistent detection metrics. Nevertheless, this method struggles with the inherent scale disparity between rotation and translation parameters, since rotational eigenvalues typically exceed translational ones by orders of magnitude, making rotational degeneracies particularly elusive to detect.

Several variants attempt to resolve the scale disparity through subspace decomposition. Methods proposed in [Rong and Michael \(2016\)](#); [Hinduja et al. \(2019\)](#); [Tagliabue et al. \(2021\)](#); [Ebadi et al. \(2023\)](#) compute relative condition numbers for translation and rotation components separately using diagonal Hessian blocks. While this provides more reliable detection without frequent retuning, it overlooks the coupling effects between translation and rotation. Similar limitations affect the diagonal block analysis in [Tuna et al. \(2023\)](#); [Chen et al. \(2024a\)](#), leading to both false positives and false negatives in degeneracy detection.

A fundamental limitation shared by these spectral methods is their inability to provide quantitative characterization of degeneracy patterns. Current approaches [Hu et al. \(2024b\)](#) incorrectly assume direct correspondence between motion parameter space (e.g., X/Y/Z axes) and eigenspace, neglecting the difference in their basis vectors. This misconception leads to imprecise characterizations such as "X-axis degeneracy" and subsequently compromises mitigation strategies. Furthermore, the inherent ambiguity of eigenvectors from EVD/SVD causes eigenvalues to lose their parameter space correspondence when sorted, particularly problematic in scenarios with combined ill-conditioning across multiple motion directions.

2.1.2 Adaptive Modeling Methods Adaptive modeling methods employ probabilistic or data-driven techniques for degeneracy detection. [Hatleskog and Alexis \(2024\)](#); ? utilize probabilistic modeling of measurement noise to calculate signal-to-noise ratios along Hessian eigenvector directions, determining degeneracy through signal strength probability definitions. While theoretically elegant, this explicit modeling

approach suffers from significant performance variations based on parameter settings for multiple noise sources and their correlations in point and normal vectors. Data-driven approaches [Nobili et al. \(2018\)](#); [Nubert et al. \(2022\)](#) implement implicit modeling for degeneracy detection. Although these methods show promise in specific scenarios, their generalization across diverse environments remains constrained by training dataset limitations. Moreover, they present significant deployment challenges on resource-constrained robotic platforms due to computational requirements.

2.2 Ill-Conditioning Mitigation

Existing mitigation strategies that do not require external sensors fall into two main categories.

2.2.1 Numerical Methods Numerical methods modify the optimization problem to address ill-conditioning. Truncated SVD [Hansen \(1990\)](#) discards components corresponding to weak singular values, effectively stabilizing solutions at the cost of information loss in potentially useful directions. Tikhonov regularization [Golub et al. \(1999\)](#) applies penalty terms uniformly across all directions, improving numerical stability but inadvertently affecting well-constrained dimensions and requiring scenario-specific parameter tuning.

[Zhang and Singh \(2014\)](#); [Zhang et al. \(2016\)](#) propose solution remapping that applies infinite penalties in ill-conditioned directions, restricting updates to well-constrained subspaces. While providing stability, this approach ignores parameter interdependencies during optimization, potentially leading to suboptimal solutions or convergence to local minima. [Tuna et al. \(2023\)](#) preprocess point correspondences by selecting observations that better constrain degenerate dimensions. Although offering targeted improvements, this method similarly discards potentially valuable information from the optimization process.

2.2.2 Robust Registration Approaches Robust registration approaches modify residual formulations through robust kernels (e.g., M-estimator, Geman-McClure, Cauchy) [Vizzo et al. \(2023\)](#); [Yang et al. \(2020\)](#) to reduce outlier influence. While effective for outlier handling, these methods do not specifically address the numerical challenges posed by ill-conditioning. Extended methods [Hatleskog and Alexis \(2024\)](#) employ probabilistic adaptive weighting for correspondences, though the use of robust kernels often compromises their probabilistic interpretation.

2.3 Research Gap

Table 1 compares the characteristics of existing methods. Current approaches exhibit three fundamental limitations that motivate our work: First, detection methods struggle with scale disparity between rotation and translation parameters while failing to properly handle their coupling effects. Second, the ambiguity in eigenvector correspondence prevents accurate characterization of degeneracy patterns in physical motion space. Third, existing mitigation methods face a trade-off between stability and information preservation, either discarding valuable information through truncation or applying uniform penalties that affect well-constrained dimensions. Most critically, current approaches treat detection and mitigation as separate, disconnected steps, lacking a unified framework that maintains the physical integrity of the optimization problem while providing targeted stabilization. Our work addresses these challenges through an integrated approach combining Schur complement decomposition for scale-aware subspace analysis (Section 4), principal direction alignment for unambiguous physical characterization (Section 5), and a solver for targeted stabilization without information loss (Section 6).

3 Problem Formulation and Preliminaries

3.1 Notations

We denote the rigid transformation as $T = \{R, t\} \in SE(3)$, comprising rotation $R \in SO(3)$ and translation $t \in \mathbb{R}^3$. The rotation matrix R belongs to the special orthogonal group $SO(3) := \{R \in \mathbb{R}^{3 \times 3} \mid R^T R = I, \det(R) = 1\}$. For incremental updates, we employ the minimal representation $\xi = [\phi^T, \delta t^T]^T \in \mathbb{R}^6$, where $\phi \in \mathbb{R}^3$ represents rotation in axis-angle form and $\delta t \in \mathbb{R}^3$ denotes translation increment. This vector resides in the *parameter space* or *tangent space* $T_x SE(3)$ at the current linearization point x . The mapping between ϕ and rotation matrices utilizes the exponential map $\exp: \mathfrak{so}(3) \rightarrow SO(3)$, where $\mathfrak{so}(3)$ is the Lie algebra of skew-symmetric matrices. For small rotations, we approximate $R \approx I + [\phi]_\times$, with $[\cdot]_\times$ denoting the skew-symmetric matrix operator.

For point clouds, we denote the source point set as $\mathcal{P} = \{p_i \in \mathbb{R}^3\}_{i=1}^N$ and the target point set as $\mathcal{Q} = \{q_i \in \mathbb{R}^3\}_{i=1}^M$, with corresponding unit surface normals $\{n_i \in \mathbb{R}^3\}_{i=1}^M$ where $\|n_i\| = 1$. In the optimization context, residual functions are denoted by $r \in \mathbb{R}^m$, residing in the *residual space*, where m is the number of constraints. The Jacobian matrix $J = \partial r / \partial \xi \in \mathbb{R}^{m \times 6}$ maps from the parameter space to the residual space. The Hessian matrix is defined as $H = J^T J \in \mathbb{R}^{6 \times 6}$, where the gradient vector is $g = J^T r \in \mathbb{R}^6$.

The spectral decomposition of $H = V \Lambda V^T$ defines the *eigenspace*, where columns of $V = [v_1, \dots, v_6]$ are eigenvectors forming an orthonormal basis, and $\Lambda = \text{diag}(\lambda_1, \dots, \lambda_6)$ contains eigenvalues in ascending order. The gradient g lies in the *observable subspace* $\text{range}(J^T) = \text{range}(H)$, which is spanned by eigenvectors corresponding to non-zero eigenvalues. The complement forms the *null space* or *unobservable subspace*. For numerical stability analysis, $\lambda_i(M)$ denotes the i -th eigenvalue of matrix M , and the condition number is defined as $\kappa(M) = \lambda_{\max}(M) / \lambda_{\min}(M)$.

While "ill-conditioning" typically refers to numerically unstable problems and "degeneracy" describes geometric under-constraint, the difference becomes blurred in practice. A degenerate configuration may or may not lead to numerical ill-conditioning depending on the specific scenario. Since this work addresses the geometric problem where scene-induced degeneracies manifest as numerical ill-conditioning, we use these terms interchangeably throughout the paper.

3.2 Nonlinear Point-to-Plane Registration

Point cloud registration aims to estimate the rigid transformation T that optimally aligns a source point set \mathcal{P} to a target set \mathcal{Q} . The point-to-plane error metric, widely adopted in LiDAR registration for its superior convergence properties Xu et al. (2022); He et al. (2023), minimizes:

$$E(R, t) = \sum_{i=1}^N [n_i^T (R p_i + t - q_i)]^2, \quad (1)$$

where q_i and n_i are the corresponding target point and normal within the set of size N , respectively.

To solve this nonlinear optimization problem, we employ iterative linearization. At each iteration, we approximate the transformation update using the first-order Taylor expansion of rotation. The transformed source point becomes:

$$R p_i + t \approx (I + [\phi]_\times) p_i + t = p_i - [p_i]_\times \phi + t, \quad (2)$$

where we utilize the property $[\phi]_\times p = -[p]_\times \phi$.

The linearized residual for each correspondence and its associated Jacobian are:

$$r_i = n_i^T (-[p_i]_\times \phi + \delta t + e_i), \quad (3a)$$

$$J_i = n_i^T [-[p_i]_\times \quad I_3] \in \mathbb{R}^{1 \times 6}, \quad (3b)$$

where $e_i = p_i - q_i$ is the current point-to-point error.

Stacking all residuals and Jacobians, we form the linear system $r = J \xi + r_0$, where $\xi = [\phi^T, \delta t^T]^T$ is the parameter increment. The optimal increment is obtained by solving the normal equations:

$$H \xi^* = -g, \quad (4)$$

where $H = J^T J$ and $g = J^T r_0$.

Once $\xi^* = [\phi^{*T}, \delta t^{*T}]^T$ is computed, the transformation is updated as:

$$R \leftarrow \exp([\phi^*]_\times) R, \quad (5a)$$

$$t \leftarrow t + \delta t^*. \quad (5b)$$

This process iterates until convergence, typically indicated by $\|\xi^*\| < \epsilon$ or negligible reduction in the cost function.

3.3 Spectral Analysis of Ill-Conditioning

Ill-conditioning in point cloud registration manifests when the Hessian matrix approaches singularity, causing numerical instability without strict rank deficiency Nashed et al. (2021). This phenomenon arises from two fundamental issues: parameter scale disparity and rotation-translation coupling.

The Hessian matrix from the linearized point-to-plane formulation exhibits a block structure:

$$H = \sum_{i=1}^N J_i^T J_i = \begin{bmatrix} H_{RR} & H_{Rt} \\ H_{Rt}^T & H_{tt} \end{bmatrix}, \quad (6)$$

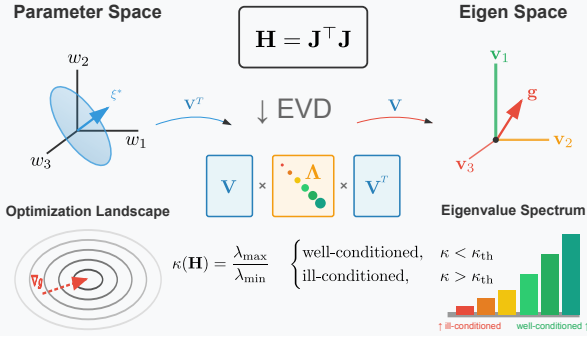


Figure 1. Physical interpretation of Hessian eigendecomposition in ICP. Transformation between parameter space and eigenspace reveals degenerate directions and their corresponding space projections, enabling principled degeneracy characterization (Section 3.3).

with sub-blocks defined as:

$$\mathbf{H}_{RR} = \sum_{i=1}^N [\mathbf{p}_i]_{\times}^{\top} \mathbf{n}_i \mathbf{n}_i^{\top} [\mathbf{p}_i]_{\times}, \quad (7a)$$

$$\mathbf{H}_{Rt} = - \sum_{i=1}^N [\mathbf{p}_i]_{\times}^{\top} \mathbf{n}_i \mathbf{n}_i^{\top}, \quad (7b)$$

$$\mathbf{H}_{tt} = \sum_{i=1}^N \mathbf{n}_i \mathbf{n}_i^{\top}. \quad (7c)$$

Scale Disparity: The rotation block \mathbf{H}_{RR} and translation block \mathbf{H}_{tt} exhibit fundamentally different scaling properties, known as the *lever arm effect* (Pomerleau et al. (2015); ?). Analysis of \mathbf{H}_{RR} reveals:

$$\|\mathbf{H}_{RR}\| \propto \sum_{i=1}^N \|\mathbf{p}_i\|^2 \sin^2(\angle(\mathbf{p}_i, \mathbf{n}_i)), \quad (8)$$

indicating that rotational constraints scale quadratically with point distances from the origin. Conversely, \mathbf{H}_{tt} depends solely on the normal distribution, independent of point distances. This creates significant scale disparity for spatially extensive point clouds.

Rotation-Translation Coupling: The off-diagonal blocks \mathbf{H}_{Rt} encode cross-coupling between rotational and translational parameters (Tuna et al. (2025)). This coupling, also scaling with point distances, causes error propagation between parameter sets and complicates the optimization landscape.

To analyze the mathematical properties of ill-conditioning, we examine the Hessian matrix through SVD, revealing the underlying geometric structure of the parameter space. The SVD of the Hessian \mathbf{H} is given by:

$$\mathbf{H} = \mathbf{U} \mathbf{\Sigma} \mathbf{V}^{\top}. \quad (9)$$

where \mathbf{U} and \mathbf{V} are orthogonal matrices containing the left and right singular vectors, and $\mathbf{\Sigma}$ is a diagonal matrix of singular values σ_i . Since \mathbf{H} is symmetric positive semi-definite (SPD), this simplifies to an eigen decomposition:

$$\mathbf{H} = \mathbf{V} \mathbf{\Lambda} \mathbf{V}^{\top}. \quad (10)$$

where \mathbf{V} contains the eigenvectors \mathbf{v}_i and $\mathbf{\Lambda}$ is a diagonal matrix of eigenvalues λ_i (with $\lambda_i = \sigma_i^2$). The geometric interpretation of this decomposition reveals the fundamental structure of the optimization landscape (Figure 1):

- Each eigenvector \mathbf{v}_i represents an orthogonal principal direction in the parameter space of ξ .
- The corresponding eigenvalue λ_i quantifies the curvature of the objective function along that direction.
- The $\mathbf{V}^{\top} \xi$ maps the parameter vector from the standard basis to the eigen space, decomposing it along the principal directions.

The gradient $\mathbf{g} = \mathbf{J}^{\top} \mathbf{r}$ resides in the observable subspace $\text{range}(\mathbf{J}^{\top}) = \text{range}(\mathbf{H})$, orthogonal to the null space. In the eigenspace, the gradient decomposes as:

$$\mathbf{g} = \sum_{i=1}^6 g_i \mathbf{v}_i, \quad \text{where } g_i = \mathbf{v}_i^{\top} \mathbf{g}, \quad (11)$$

with $g_i = 0$ for eigenvectors in the null space ($\lambda_i = 0$).

This spectral framework forms the theoretical foundation for our approach to handling ill-conditioning, encompassing ill-conditioning detection (Section 4), quantitative characterization (Section 5), and targeted mitigation (Section 6). By explicitly mapping between eigenspace and parameter space, we systematically address scale disparity and coupling effects while preserving observable information.

4 Ill-Conditioning Detection through Parameter Decoupling

In this section, we introduce our novel parameter decoupling method that reliably detects ill-conditioning. Our key insight is that by decoupling and elimination, we can independently analyze the constraint of rotation and translation, thereby avoiding interference from scale disparity and coupling effects, resulting in clean information for each subproblem.

4.1 Understanding Ill-conditioning through Condition Number

To understand the physical meaning of ill-conditioning (Tuna et al. (2025); Golub and Van Loan (2013)), we begin with the update step in optimization (Equation (4)):

$$\xi^* = -\mathbf{H}^{-1} \mathbf{g} = -\mathbf{V} \mathbf{\Lambda}^{-1} \mathbf{V}^{\top} \mathbf{g} = - \sum_{i=1}^6 \frac{\mathbf{v}_i^{\top} \mathbf{g}}{\lambda_i} \mathbf{v}_i, \quad (12)$$

Now consider a small perturbation $\Delta(-\mathbf{g})$ in the right-hand side due to sensor noise or measurement errors. This causes a corresponding error in the solution $\Delta \xi^*$:

$$\|\Delta \xi^*\| \leq \|\mathbf{H}^{-1}\| \cdot \|\Delta(-\mathbf{g})\| = \frac{1}{\lambda_{\min}} \cdot \|\Delta(-\mathbf{g})\|, \quad (13)$$

where λ_{\min} is the smallest eigenvalue of \mathbf{H} . Similarly, for the original system:

$$\|\xi^*\| \geq \frac{1}{\|\mathbf{H}\|} \cdot \|\mathbf{g}\| = \frac{1}{\lambda_{\max}} \cdot \|\mathbf{g}\|, \quad (14)$$

where λ_{\max} is the largest eigenvalue of \mathbf{H} . Combining these inequalities:

$$\frac{\|\Delta \xi^*\|}{\|\xi^*\|} \leq \frac{\lambda_{\max}}{\lambda_{\min}} \cdot \frac{\|\Delta(-\mathbf{g})\|}{\|\mathbf{g}\|}, \quad (15)$$

This ratio of eigenvalues appears naturally in our error analysis, defining the condition number: $\kappa(\mathbf{H}) = \lambda_{\max}/\lambda_{\min}$.

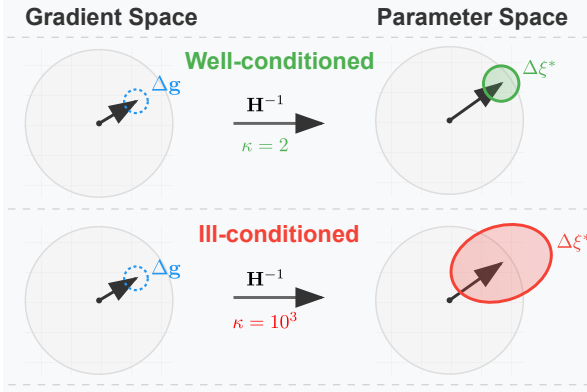


Figure 2. The error amplification effect in ill-conditioning. Visualization of how condition number determines the upper bound on relative parameter error given relative perturbations in the optimization space (Section 4.1).

The error bound now becomes:

$$\frac{\|\Delta \xi^*\|}{\|\xi^*\|} \leq \kappa(H) \cdot \frac{\|\Delta(-g)\|}{\|g\|}. \quad (16)$$

This inequality reveals the fundamental importance of condition number: it acts as an error amplifier. When $\kappa(H)$ is large, even small relative perturbations in the input can lead to large relative errors in the solution (Figure 2).

From Equation (12), we can see why this happens, directions with small eigenvalues receive updates scaled by $1/\lambda_i$, making them sensitive to noise. Therefore, the condition number provides a quantitative measure for detecting ill-conditioning. A large condition number indicates the system is ill-conditioned, with some directions much more weakly constrained than others, making the solution unstable and unreliable. With this understanding, we present our parameter decoupling approach for reliable conditioning analysis discussed below.

4.2 Subspace Decoupling via Schur Complement

Traditional ill-conditioning detection approaches Tuna et al. (2023); Hu et al. (2024b) have either analyzed the full Hessian matrix or examined its diagonal blocks in isolation. However, isolated analysis proves insufficient. Analyzing $\kappa(H_{RR})$ merely reflects how well the point cloud constrains rotation under fixed translation, while $\kappa(H_{tt})$ measures translation constraints under fixed rotation. This approach overestimates the effective curvature and the actual constraint strength, also underestimates the magnitude of ill-conditioning, leading to false negatives for degeneracy caused by rotation-translation coupling. Even when both $\kappa(H_{RR})$ and $\kappa(H_{tt})$ appear well-conditioned, the overall system can exhibit severe ill-conditioning due to strong rotation-translation coupling. Therefore, we must analyze rotation and translation constraints separately while properly accounting for their coupling effects in subspace. The *Schur complement* provides the ideal mathematical framework for this decoupling. For a general block matrix:

$$M = \begin{bmatrix} A & B \\ C & D \end{bmatrix}, \quad S_A = A - BD^{-1}C. \quad (17)$$

where D is assumed invertible, the *Schur complement* with respect to block D is defined as S_A . This operation eliminates

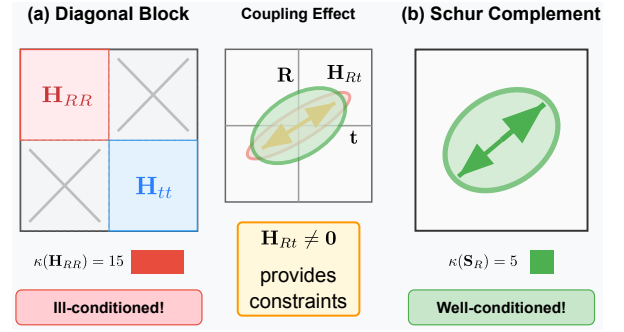


Figure 3. Visualization of rotation-translation coupling effect on ill-conditioning detection. (a) Traditional diagonal subspace decoupling ignores cross-coupling terms, which may hide existing ill-conditioning. (b) *Schur complement* decoupling properly isolates subspaces by accounting for coupling effects, enabling reliable degeneracy detection in the clean parameter subspace (Section 4.2).

variables associated with D while preserving their influence on variables in block A .

Applying this principle to the Hessian matrix yields the rotation and translation *Schur complements*:

$$S_R = H_{RR} - M_R, \quad (18a)$$

$$S_t = H_{tt} - M_t, \quad (18b)$$

$$M_R = H_{Rt} H_{tt}^{-1} H_{tR}, \quad (18c)$$

$$M_t = H_{tR} H_{RR}^{-1} H_{Rt}. \quad (18d)$$

The correction terms M_R and M_t quantify the bidirectional influence between rotation and translation, potentially revealing ill-conditioning that remains hidden in isolated analysis when strong coupling exists. The condition numbers of these *Schur complements*, reveal the effective curvature and true sensitivity after optimally accommodating the complementary motion components (Theorem 1). In the Jacobian space, this is equivalent to orthogonally removing components explicable by the complementary subspace (Proposition 1), while maintaining strict invariance to uniform scaling of the eliminated block (Proposition 2). Consequently, our decoupled methods can provide insights that conventional analysis would miss.

4.3 Normalized Eigenvalue in Decoupled Subspaces

The decoupled subspaces provide a foundation for reliable ill-conditioning detection. Beyond merely identifying which parameter subspace exhibits ill-conditioning, we can pinpoint the specific physical directions most vulnerable to numerical instability. We begin by extracting the eigen structure of the *Schur complement* matrices:

$$S_R = V_R \Lambda_R V_R^T, \quad S_t = V_t \Lambda_t V_t^T, \quad (19)$$

where $\Lambda_R = \text{diag}(\lambda_{R,1}, \lambda_{R,2}, \lambda_{R,3})$ and $\Lambda_t = \text{diag}(\lambda_{t,1}, \lambda_{t,2}, \lambda_{t,3})$ contain the eigenvalues in ascending order. The columns of V_R and V_t represent the principal directions of constraint in the rotation and translation parameter spaces.

Then we compute normalized eigenvalues to identify direction-specific vulnerabilities:

$$\kappa_{R,i} = \frac{\lambda_{R,3}}{\lambda_{R,i}}, \quad \kappa_{t,i} = \frac{\lambda_{t,3}}{\lambda_{t,i}}, \quad (20)$$

Algorithm 1 Direction-Specific Ill-Conditioning Detection

```

1: Input: Hessian  $\mathbf{H}$  with blocks  $\mathbf{H}_{RR}, \mathbf{H}_{tt}, \mathbf{H}_{Rt}, \mathbf{H}_{tR}$ ;
   threshold  $\kappa_{th}$ 
2: Output: Ill-conditioned directions  $\{\mathbf{V}_R^{ill}, \mathbf{V}_t^{ill}\}$ 
3:  $\mathbf{S}_R \leftarrow \mathbf{H}_{RR} - \mathbf{H}_{Rt}\mathbf{H}_{tt}^{-1}\mathbf{H}_{tR}$  ▷ Equation (18a)
4:  $\mathbf{S}_t \leftarrow \mathbf{H}_{tt} - \mathbf{H}_{tR}\mathbf{H}_{RR}^{-1}\mathbf{H}_{Rt}$  ▷ Equation (18b)
5:  $\{\lambda_{R,i}, \mathbf{V}_{R,i}\}_{i=1}^3 \leftarrow \text{EVD}(\mathbf{S}_R)$  (asc.)
6:  $\{\lambda_{t,i}, \mathbf{V}_{t,i}\}_{i=1}^3 \leftarrow \text{EVD}(\mathbf{S}_t)$  (asc.)
7:  $\mathbf{V}_R^{ill} \leftarrow \emptyset, \mathbf{V}_t^{ill} \leftarrow \emptyset$ 
8: for  $i = 1$  to 3 do
9:    $\kappa_{R,i} \leftarrow \lambda_{R,3}/\lambda_{R,i}$ 
10:   $\kappa_{t,i} \leftarrow \lambda_{t,3}/\lambda_{t,i}$ 
11:  if  $\kappa_{R,i} > \kappa_{th}$  then  $\mathbf{V}_R^{ill} \leftarrow \mathbf{V}_R^{ill} \cup \{\mathbf{V}_{R,i}\}$ 
12:  end if
13:  if  $\kappa_{t,i} > \kappa_{th}$  then  $\mathbf{V}_t^{ill} \leftarrow \mathbf{V}_t^{ill} \cup \{\mathbf{V}_{t,i}\}$ 
14:  end if
15: end for
16: return  $\{\mathbf{V}_R^{ill}, \mathbf{V}_t^{ill}\}$ 

```

where $\kappa_{R,i}$ and $\kappa_{t,i}$ are the normalized eigenvalues for rotation and translation, respectively. This formulation resembles direction-specific condition numbers, with the largest eigenvalue divided by each individual eigenvalue. Larger values of $\kappa_{R,i}$ or $\kappa_{t,i}$ indicate weaker constraints in the corresponding directions.

We then identify ill-constrained directions using a threshold on these normalized eigenvalues:

$$\kappa_{R,i} > \kappa_{th} \text{ OR } \kappa_{t,i} > \kappa_{th}. \quad (21)$$

where κ_{th} is a threshold typically set between 10 and 50. The corresponding eigenvectors indicate the specific physical directions requiring regularization.

By analyzing these direction-specific condition numbers, we gain precise insight into which specific motion components are poorly constrained, enabling targeted stabilization strategies (Algorithm 1).

4.4 Theoretical Foundation for Schur Conditioning

We establish the theoretical foundation for *Schur complement* conditioning under the following default assumptions. Unless otherwise specified, we assume $\mathbf{H}_{tt} \succ 0$ and $\mathbf{H}_{RR} \succ 0$, so that \mathbf{S}_R and \mathbf{S}_t are well-defined (Generalizations using the Moore-Penrose inverse).

Theorem 1. Elimination-Curvature Equivalence. *For the Hessian \mathbf{H} , the Schur complements \mathbf{S}_R and \mathbf{S}_t satisfy:*

- (i) *The reduced quadratic after eliminating $\delta\mathbf{t}$ has Hessian \mathbf{S}_R :*

$$Q(\phi) = \frac{1}{2}\phi^\top \mathbf{S}_R \phi - \tilde{\mathbf{g}}_R^\top \phi + \text{const} \quad (22)$$

- (ii) *Under perturbation $\Delta\tilde{\mathbf{g}}_R$ in the reduced gradient:*

$$\frac{\|\Delta\phi^*\|_2}{\|\phi^*\|_2} \leq \kappa(\mathbf{S}_R) \cdot \frac{\|\Delta\tilde{\mathbf{g}}_R\|_2}{\|\tilde{\mathbf{g}}_R\|_2} \quad (23)$$

Analogous results hold for \mathbf{S}_t when eliminating ϕ .

Proof: See Section A.1.

This theorem demonstrates that rotation and translation sensitivities are governed by \mathbf{S}_R and \mathbf{S}_t , with their condition numbers $\kappa(\mathbf{S}_R)$ and $\kappa(\mathbf{S}_t)$ bounding the relative error amplification. That is, \mathbf{S}_R is precisely the Hessian of the rotation subproblem after optimally accommodating translation; hence spectral analysis on the rotation subproblem is equivalent (the sensitivity of ϕ) to analyzing the full problem with $\delta\mathbf{t}$ eliminated. This property enables *Schur complements* to expose hidden degeneracy by optimally accounting for inter-block coupling degeneracy that remain invisible when analyzing diagonal blocks in isolation.

Proposition 1. Projection Representation. *Consider the Jacobian matrix $\mathbf{J} = [\mathbf{J}_R \mid \mathbf{J}_t] \in \mathbb{R}^{m \times 6}$, where $\mathbf{J}_R \in \mathbb{R}^{m \times 3}$ and $\mathbf{J}_t \in \mathbb{R}^{m \times 3}$ represent the rotational and translational components, respectively. Let \mathbf{P}_t denote the orthogonal projection operator onto $\text{range}(\mathbf{J}_t)$ with Moore-Penrose pseudoinverse, given by*

$$\mathbf{P}_t \triangleq \mathbf{J}_t \mathbf{J}_t^+. \quad (24)$$

Then, the rotational stiffness matrix \mathbf{S}_R can be expressed as

$$\mathbf{S}_R = \mathbf{J}_R^\top (\mathbf{I}_m - \mathbf{P}_t) \mathbf{J}_R, \quad (25)$$

where $\mathbf{I}_m \in \mathbb{R}^{m \times m}$ is the identity matrix, and $(\mathbf{I}_m - \mathbf{P}_t)$ projects onto the orthogonal complement of $\text{range}(\mathbf{J}_t)$.

For the weighted case with positive definite information matrix $\mathbf{W} \succ 0$, the corresponding \mathbf{W} -orthogonal projector is given by $\mathbf{P}_t^{(\mathbf{W})} \triangleq \mathbf{J}_t (\mathbf{J}_t^\top \mathbf{W} \mathbf{J}_t)^+ \mathbf{J}_t^\top \mathbf{W}$, and the weighted rotational stiffness matrix becomes

$$\mathbf{S}_R = \mathbf{J}_R^\top \mathbf{W} (\mathbf{I}_m - \mathbf{P}_t^{(\mathbf{W})}) \mathbf{J}_R, \quad (26)$$

where the projections are performed with respect to the \mathbf{W} -inner product $\langle \mathbf{u}, \mathbf{v} \rangle_{\mathbf{W}} = \mathbf{u}^\top \mathbf{W} \mathbf{v}$.

Proof: See Section A.2.

This projection removes components of $\text{range}(\mathbf{J}_R)$ that can be explained by \mathbf{J}_t , retaining only the rotation information that cannot be compensated by translation. Consequently, the eigenvalues of \mathbf{S}_R in the projected subspace accurately reflect the rotational information of the corresponding subproblem.

Proposition 2. Scale- and Orthogonal-Basis Invariance. *The Schur complements exhibit scale and orthogonal-basis invariance:*

- (i) **(Scale invariance)** *For any $s > 0$, if $\delta\mathbf{t}' = s\delta\mathbf{t}$ so that $\mathbf{H}_{tt} \mapsto s^2\mathbf{H}_{tt}$ and $\mathbf{H}_{Rt} \mapsto s\mathbf{H}_{Rt}$, then $\mathbf{S}_R' = \mathbf{S}_R$.*
- (ii) **(Orthogonal-basis invariance)** *If the retained block undergoes an orthogonal change of basis $\mathbf{J}_R \mapsto \mathbf{J}_R \mathbf{Q}$ with $\mathbf{Q} \in \text{SO}(3)$, then $\mathbf{S}_R \mapsto \mathbf{Q}^\top \mathbf{S}_R \mathbf{Q}$, preserving the spectrum and thus $\kappa(\mathbf{S}_R)$.*

Analogous results hold for \mathbf{S}_t and $\kappa(\mathbf{S}_t)$.

Proof: See Section A.3.

This property demonstrates that *Schur complements* naturally eliminate sensitivity to unit or scale changes in the eliminated parameters, directly addressing the scale disparity between rotation (radians) and translation (meters). If the translation unit is rescaled as $\mathbf{t} \leftarrow s\mathbf{t}$ with $s > 0$, the Hessian

blocks transform proportionally as $\mathbf{H}_{tt} \sim s^2$ and $\mathbf{H}_{Rt} \sim s$. These factors cancel in \mathbf{M}_R , hence \mathbf{S}_R is invariant to this scaling. More general (non-orthogonal) re-parameterizations do not necessarily preserve the condition number.

Theorem 2. Spectral Bounds for Schur Conditioning. Let \mathbf{M}_R and \mathbf{M}_t denote the coupling matrices, $\mathbf{M}_R \succeq \mathbf{0}$ and $\mathbf{M}_t \succeq \mathbf{0}$, the spectral properties satisfy:

(i) **Loewner ordering:** $\mathbf{S}_R \preceq \mathbf{H}_{RR}$ and $\mathbf{S}_t \preceq \mathbf{H}_{tt}$,

(ii) **Eigenvalue bounds:** For $i \in \{1, 2, 3\}$,

$$\lambda_i(\mathbf{H}_{RR}) - \lambda_{\max}(\mathbf{M}_R) \leq \lambda_i(\mathbf{S}_R) \quad (27)$$

$$\leq \lambda_i(\mathbf{H}_{RR}). \quad (28)$$

(iii) **Condition number bounds:** Under the assumption $\lambda_{\min}(\mathbf{H}_{RR}) > \lambda_{\max}(\mathbf{M}_R)$,

$$\kappa(\mathbf{S}_R) \leq \frac{\lambda_{\max}(\mathbf{H}_{RR})}{\lambda_{\min}(\mathbf{H}_{RR}) - \lambda_{\max}(\mathbf{M}_R)} \quad (29)$$

(iv) **Near-cancellation:** Let $\mathbf{v}_* \in \mathbb{S}^2$ attain the minimum Rayleigh quotient of \mathbf{S}_R . Then

$$\mathbf{v}_*^\top \mathbf{M}_R \mathbf{v}_* = \mathbf{v}_*^\top \mathbf{H}_{RR} \mathbf{v}_* - \lambda_{\min}(\mathbf{S}_R) \quad (30)$$

$$\geq \lambda_{\min}(\mathbf{H}_{RR}) - \lambda_{\min}(\mathbf{S}_R). \quad (31)$$

Hence, if $\lambda_{\min}(\mathbf{S}_R) \ll \lambda_{\min}(\mathbf{H}_{RR})$, the coupling term nearly cancels the rotational curvature along \mathbf{v}_* :

$$\frac{\mathbf{v}_*^\top \mathbf{M}_R \mathbf{v}_*}{\mathbf{v}_*^\top \mathbf{H}_{RR} \mathbf{v}_*} \geq 1 - \frac{\lambda_{\min}(\mathbf{S}_R)}{\mathbf{v}_*^\top \mathbf{H}_{RR} \mathbf{v}_*} \quad (32)$$

$$\geq 1 - \frac{\lambda_{\min}(\mathbf{S}_R)}{\lambda_{\min}(\mathbf{H}_{RR})}. \quad (33)$$

Analogous results hold for \mathbf{S}_t , $\kappa(\mathbf{S}_t)$ and $\lambda_i(\mathbf{S}_t)$.

Proof: See Section A.4.

Remark 1. From (i) and (ii), \mathbf{S}_R and \mathbf{S}_t are not guaranteed to be better-conditioned than their diagonal block \mathbf{H}_{RR} and \mathbf{H}_{tt} . As the Loewner ordering ? implies that:

$$\lambda_{\min}(\mathbf{S}_R) \leq \lambda_{\min}(\mathbf{H}_{RR}), \quad \lambda_{\max}(\mathbf{S}_R) \leq \lambda_{\max}(\mathbf{H}_{RR}).$$

Consequently, $\kappa(\mathbf{S}_R)$ may be smaller than $\kappa(\mathbf{H}_{RR})$ when coupling is weak, or substantially larger when coupling is strong. So the *Schur complements* can reveal *hidden degeneracy* induced by coupling: even when the diagonal block appears well-conditioned, subtracting the coupling \mathbf{M}_R may reduce the smallest eigenvalue, inflating $\kappa(\mathbf{S}_R)$.

Remark 2. (iii) provides a finite upper bound for the SPD regime; As $\lambda_{\max}(\mathbf{M}_R) \rightarrow \lambda_{\min}(\mathbf{H}_{RR})$, we have $\kappa(\mathbf{S}_R) \rightarrow \infty$, revealing degeneracy masked by diagonal-block analysis.

Remark 3. (iv) shows that the real observability information can be masked by the cross terms (\mathbf{M}_R and \mathbf{M}_t). This constitutes the degeneration mechanism being "covered" on \mathbf{H}_{RR} , observable only in \mathbf{S}_R . Finally, it gives a quantitative form of the "masking" mechanism.

5 Resolving Eigenvector Ambiguity with Principled Alignment

Building upon the decoupled analysis in Section 4.2, we now address the challenge of mapping abstract eigenvectors to physical motion parameters. While our *Schur complement* approach successfully eliminate the coupling effect in subspaces, the eigenvectors obtained from these decoupled matrices require further interpretation to guide practical regularization strategies.

Let $\mathcal{E}_R = \{\mathbf{v}_{R,1}, \mathbf{v}_{R,2}, \mathbf{v}_{R,3}\}$ and $\mathcal{E}_t = \{\mathbf{v}_{t,1}, \mathbf{v}_{t,2}, \mathbf{v}_{t,3}\}$ represent the eigenvector sets from our *Schur complement* analysis, sorted by ascending eigenvalues. In practical robotics scenarios, these eigenvectors exhibit three forms of ambiguity that complicate physical interpretation:

- **Sign ambiguity:** The arbitrary sign of eigenvectors (\mathbf{v} or $-\mathbf{v}$) creates inconsistent physical interpretations. For instance, a robot's rotational uncertainty around the vertical axis could be represented by either $\mathbf{v} = [0, 0, 1]^\top$ or $\mathbf{v} = [0, 0, -1]^\top$, though they represent the same physical constraint.
- **Ordering ambiguity:** In corridor-like environments, where motion x and roll are similarly constrained, corresponding eigenvalues become nearly identical or the spectral gap is small, making their natural ordering unstable across iterations or frames.
- **Basis ambiguity:** In planar scenarios, where the robot may be constrained to move in the horizontal plane, multiple linearly independent vectors within this plane could equally represent the degenerate subspace, leading to arbitrary basis choices by the eigen decomposition.

In this section, we present a principled alignment framework comprising three steps (Figure 4 and Algorithm 2): inner-product matching (Section 5.1), maximum component analysis (Section 5.2), and *Gram-Schmidt orthogonalization* (Section 5.3) to address these ambiguities.

5.1 Inner-product Matching

We first establish that any eigenvector can be expressed as a linear combination of standard parameter axes $\{\mathbf{e}_x, \mathbf{e}_y, \mathbf{e}_z\}$ corresponding to the canonical basis in \mathbb{R}^3 :

$$\mathbf{v} = v_1 \mathbf{e}_x + v_2 \mathbf{e}_y + v_3 \mathbf{e}_z, \quad (34)$$

where v_i are the projection coefficients that determine the contribution of each canonical direction.

Our alignment framework begins by addressing sign ambiguity through inner-product matching. For each eigenvector $\mathbf{v}_{R,i} \in \mathcal{E}_R$ and $\mathbf{v}_{t,i} \in \mathcal{E}_t$, we compute alignment coefficients with the canonical basis $\{\mathbf{e}_x, \mathbf{e}_y, \mathbf{e}_z\}$:

$$\alpha_{R,i,j} = \|\mathbf{v}_{R,i} \cdot \mathbf{e}_j\| = \|v_j\| = \cos \theta_{ij}, \quad \forall j \in \{x, y, z\}, \quad (35a)$$

$$\alpha_{t,i,j} = \|\mathbf{v}_{t,i} \cdot \mathbf{e}_j\| = \|v_j\| = \cos \theta_{ij}, \quad \forall j \in \{x, y, z\}. \quad (35b)$$

where θ_{ij} represents the angle between eigenvector \mathbf{v}_i and canonical axis \mathbf{e}_j .

This geometric interpretation provides intuitive understanding: larger values of $\|v_j\|$ indicate smaller angles, meaning the eigenvector is more aligned with that axis. The absolute value ensures invariance to arbitrary sign flips in eigen

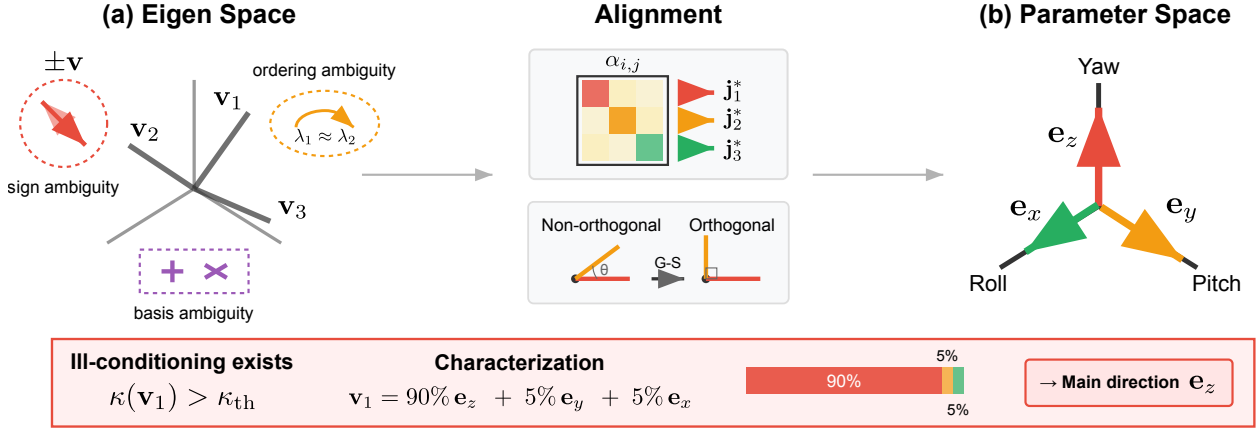


Figure 4. Pipeline for quantitative ill-conditioning characterization. The three-stage process addresses eigenvector ambiguities in optimization subspaces: (1) Inner product matching resolves sign ambiguity and determines linear combinations in parameter space (Section 5.1); (2) Maximum component analysis resolves ordering ambiguity to identify principal axis alignment (Section 5.2); (3) Gram-Schmidt orthogonalization resolves basis ambiguity, producing a stable orthonormal basis aligned with the parameter space for subsequent degeneracy mitigation (Section 5.3).

Algorithm 2 Characterization of Ill-conditioning

```

1: Input:  $\mathcal{E}_R = \{v_{R,i}\}_{i=1}^3$ ,  $\mathcal{E}_t = \{v_{t,i}\}_{i=1}^3$ 
2: Output:  $\mathcal{P}_R$ ,  $\mathcal{P}_t$ 
3:  $\mathcal{P}_R \leftarrow \emptyset$ ,  $\mathcal{P}_t \leftarrow \emptyset$ 
4: % Inner-product matching ▷ Equations (35a) to (35b)
5: for  $i = 1$  to  $3$  do
6:   for  $j \in \{x, y, z\}$  do
7:      $\alpha_{R,i,j} \leftarrow \|v_{R,i} \cdot e_j\|$ ,  $\alpha_{t,i,j} \leftarrow \|v_{t,i} \cdot e_j\|$ 
8:   end for
9:   % Maximum component analysis ▷ Equations (36) to (37)
10:   $j_{R,i}^* \leftarrow \arg \max_j \alpha_{R,i,j}$ ,  $j_{t,i}^* \leftarrow \arg \max_j \alpha_{t,i,j}$ 
11:  % Alignment strength ▷ Equations (38a) to (38b)
12:   $\gamma_{R,i} \leftarrow \max_j \alpha_{R,i,j}$ ,  $\gamma_{t,i} \leftarrow \max_j \alpha_{t,i,j}$ 
13: end for
14: % Gram-Schmidt orthogonalization ▷ Equation (40)
15: for  $i = 1$  to  $3$  do
16:   $v'_{R,i} \leftarrow v_{R,i} - \sum_{k=1}^{i-1} (v_{R,i} \cdot p_{R,k}) p_{R,k}$ 
17:   $p_{R,i} \leftarrow v'_{R,i} / \|v'_{R,i}\|$ 
18:   $v'_{t,i} \leftarrow v_{t,i} - \sum_{k=1}^{i-1} (v_{t,i} \cdot p_{t,k}) p_{t,k}$ 
19:   $p_{t,i} \leftarrow v'_{t,i} / \|v'_{t,i}\|$ 
20:   $\mathcal{P}_R \leftarrow \mathcal{P}_R \cup \{p_{R,i}\}$ ,  $\mathcal{P}_t \leftarrow \mathcal{P}_t \cup \{p_{t,i}\}$ 
21: end for
22: return  $\mathcal{P}_R$ ,  $\mathcal{P}_t$ ,  $\{j_{R,i}^*\}$ ,  $\{j_{t,i}^*\}$ ,  $\{\gamma_{R,i}\}$ ,  $\{\gamma_{t,i}\}$ 

```

decomposition. This yields normalized alignment coefficients $\alpha_{R,i,j}, \alpha_{t,i,j} \in [0, 1]$ that quantify projection magnitude onto each physical axis. These coefficients form the foundation for subsequent alignment steps by establishing initial relationship between eigenvectors and physical parameter space.

5.2 Maximum Component Analysis

The second step addresses ordering ambiguity through maximum component analysis. For each eigenvector, we identify its dominant physical axis alignment:

$$j_{R,i}^* = \arg \max_{j \in \{x,y,z\}} \alpha_{R,i,j}, \quad j_{t,i}^* = \arg \max_{j \in \{x,y,z\}} \alpha_{t,i,j}, \quad (36)$$

To provide a more intuitive relative measure, we compute the contribution percentage of each component:

$$c_j = \frac{\|v_j\|}{\sum_{i=1}^3 \|v_i\|}, \quad j \in \{x, y, z\}, \quad (37)$$

which reflects the relative magnitude of components. For instance, if $c_z \approx 90\%$, the eigenvector primarily contributes along e_z (corresponding to yaw or vertical translation).

This operation establishes a consistent mapping criterion between eigenvectors and physical axes. The ill-conditioned direction characterized by $v_{R,1}$ (associated with the smallest eigenvalue $\lambda_{R,1}$) is thus identified with physical rotation axis $j_{R,1}^*$. The strength of alignment is quantified by:

$$\gamma_{R,i} = \alpha_{R,i,j_{R,i}^*} = \max_j \alpha_{R,i,j}, \quad (38a)$$

$$\gamma_{t,i} = \alpha_{t,i,j_{t,i}^*} = \max_j \alpha_{t,i,j}. \quad (38b)$$

When $\gamma_{R,i}$ or $\gamma_{t,i}$ approaches 1, the eigenvector closely aligns with a single physical axis, providing clear physical interpretation. When significantly below 1, the ill-conditioning affects a complex combination of physical axes, requiring further orthogonalization to resolve the basis ambiguity. This mapping allows us to understand which physical degrees of freedom each eigenvector primarily represents, providing a foundation for targeted regularization that is more precise than using raw eigenvectors which may represent arbitrary linear combinations of physical axes.

5.3 Gram-Schmidt Orthogonalization

The third step addresses basis ambiguity, particularly when multiple eigenvalues are similar or with small spectral gap. When *eigenvalue clustering* occurs (i.e., $\lambda_{R,i} \approx \lambda_{R,j}$), the corresponding eigenvectors become numerically unstable and their orientations can vary significantly between iterations. This instability arises because while the invariant subspace $\mathcal{S}_R = \text{span}\{v_{R,i}, v_{R,j}\}$ remains well-defined, individual eigenvectors within it are not uniquely determined ???. According to the *Davis-Kahan theorem*, the angular deviation of computed eigenvectors satisfies:

$$\|\sin \Theta(U, \tilde{U})\|_2 \leq \frac{\|\Delta\|_2}{\delta} \quad (39)$$

where $\delta = \min_{i \neq j} \|\lambda_i - \lambda_j\|$ denotes the minimum spectral gap between distinct eigenvalue clusters, Δ represents the perturbation matrix, and $\Theta(U, \tilde{U})$ measures the canonical angles between the true and computed eigenspaces.

To establish a stable and consistent basis for subsequent processing, we construct canonical orthogonal bases $\mathcal{P}_R =$

Algorithm 3 Preconditioned Conjugate Gradient

```

1: Input:  $H, g, \{\lambda_{R,i}, V_{R,i}\}, \{\lambda_{t,i}, V_{t,i}\}, \kappa_{tg}$ 
2: Output: Optimized parameter update  $\Delta\xi$ 
3: % Construct preconditioner ▷ Equations (43) to (46)
4:  $\tilde{\lambda}_i \leftarrow \max(\lambda_i, \lambda_{\max}/\kappa_{tg}) \quad \forall i \in \{1, 2, 3\}$ 
5:  $P \leftarrow \text{blkdiag}(V_R \tilde{\Lambda}_R^{-1} V_R^\top, V_t \tilde{\Lambda}_t^{-1} V_t^\top)$ 
6: % Solving PCG
7:  $r_0 \leftarrow -g, z_0 \leftarrow P^{-1} r_0, p_0 \leftarrow z_0, \Delta\xi_0 \leftarrow 0$ 
8: for  $k = 0$  to convergence do
9:    $\alpha_k \leftarrow r_k^\top z_k / p_k^\top H p_k$  ▷ Step size
10:   $\Delta\xi_{k+1} \leftarrow \Delta\xi_k + \alpha_k p_k$  ▷ Update parameters
11:   $r_{k+1} \leftarrow r_k - \alpha_k H p_k$  ▷ Update residual
12:   $z_{k+1} \leftarrow P^{-1} r_{k+1}$  ▷ Targeted preconditioning
13:   $\beta_k \leftarrow r_{k+1}^\top z_{k+1} / r_k^\top z_k$  ▷ Conjugacy coefficient
14:   $p_{k+1} \leftarrow z_{k+1} + \beta_k p_k$  ▷ New search direction
15: end for
16: return  $\Delta\xi_{k+1}$ 

```

$\{p_{R,1}, p_{R,2}, p_{R,3}\}$ and $\mathcal{P}_t = \{p_{t,1}, p_{t,2}, p_{t,3}\}$ aligned with physical axes through Gram-Schmidt orthogonalization. The process prioritizes the eigenvector most strongly aligned with a physical axis:

$$v'_{R,i} = v_{R,i} - \sum_{k=1}^{i-1} (v_{R,i} \cdot p_{R,k}) p_{R,k} \quad (40a)$$

$$p_{R,i} = \|v'_{R,i}\|^{-1} v'_{R,i} \quad (40b)$$

$$v'_{t,i} = v_{t,i} - \sum_{k=1}^{i-1} (v_{t,i} \cdot p_{t,k}) p_{t,k} \quad (40c)$$

$$p_{t,i} = \|v'_{t,i}\|^{-1} v'_{t,i} \quad (40d)$$

For rotation subspaces with eigenvalue multiplicity $m > 1$ (indicating m -dimensional degenerate subspaces), our orthogonalization ensures the resulting basis $\{p_{R,1}, p_{R,2}, \dots, p_{R,m}\}$ maintains maximum alignment with physical axes while preserving the invariant subspace spanned by the original eigenvectors. This canonical basis construction provides numerical stability and interpretability for the eigenvalue clamping strategy detailed in the following section.

6 Targeted Ill-Conditioning Mitigation via Eigenvalue Clamping

Building upon our detection (Section 4) and principled alignment methodology (Section 5), we now develop a targeted stabilization approach that selectively addresses ill-conditioned directions while preserving natural convergence behavior in well-constrained dimensions (Algorithm 3).

6.1 Preconditioned Conjugate Gradient

The iterative optimization in point cloud registration requires solving the normal equation in Equation (3a) at each step. Traditional Tikhonov regularization ($(H + \lambda I)\Delta\xi = -g$) apply uniform damping across all parameters, unnecessarily impeding convergence in well-conditioned directions. Truncation methods, conversely, completely discard information in ill-conditioned directions, sacrificing potentially useful gradient information (Figure 5).

The Preconditioned Conjugate Gradient (PCG) algorithm ?? implicitly works with this transformed system while

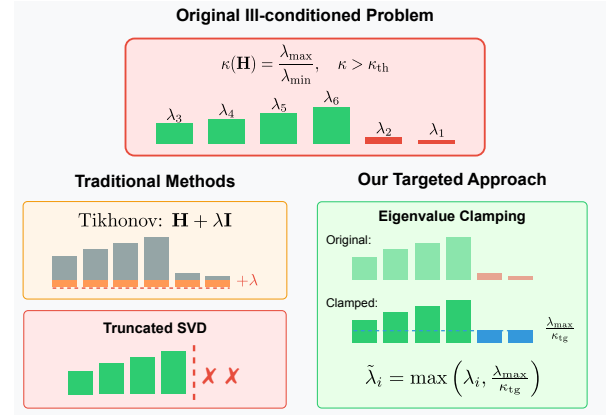


Figure 5. Algorithmic principles for mitigating ill-conditioned optimization. Visualization of how different methods modify the solution space to mitigate numerical degeneracy in point cloud registration.

returning the solution in the original parameter space. Crucially, its convergence rate depends on the condition number of the preconditioned system $\kappa(P^{-1}H)$ rather than $\kappa(H)$ according to Section 4.1. The key insight of PCG is to solve the original system $H\Delta\xi = -g$ by implicitly working with a transformed, better-conditioned system. Given a left preconditioner $P \approx H^{-1}$, PCG effectively solves:

$$\underbrace{(PH)}_{\text{Well-conditioned}} \Delta\xi = P(-g) \quad (41)$$

The crucial property is that the convergence rate depends on $\kappa(PH)$ rather than $\kappa(H)$. When P is well-designed, $\kappa(PH) \ll \kappa(H)$, leading to dramatically stable and faster convergence. The PCG algorithm achieves this transformation implicitly through the key preconditioning step:

$$z_k = P r_k \quad (42)$$

where $r_k = -g - H\Delta\xi_k$ is the residual. This step approximates the Newton direction $H^{-1}r_k$, rescaling the search space to balance poorly and well-conditioned directions.

6.2 Targeted Preconditioner Design

The effectiveness of PCG hinges on the preconditioner design. Leveraging our physically-aligned eigen decompositions from Section 5, we construct a block-diagonal preconditioner:

$$P = \begin{bmatrix} P_R & 0 \\ 0 & P_t \end{bmatrix} \quad (43)$$

where each block approximates the inverse of the corresponding Schur complement:

$$P_R = V_R \tilde{\Lambda}_R^{-1} V_R^\top, \quad P_t = V_t \tilde{\Lambda}_t^{-1} V_t^\top \quad (44)$$

In practice, to avoid explicit inversion in the PCG algorithm, we store and use the inverse of the preconditioner:

$$P^{-1} = \begin{bmatrix} V_R \tilde{\Lambda}_R V_R^\top & 0 \\ 0 & V_t \tilde{\Lambda}_t V_t^\top \end{bmatrix} \quad (45)$$

This allows efficient computation of z_k in the PCG iteration.

The critical element is the adjustment of eigenvalues to mitigate ill-conditioning while preserving information. Unlike

uniform regularization that penalizes all directions equally, we introduce a κ_{tg} eigenvalue clamping strategy:

$$\tilde{\lambda}_i = f(\lambda_i) = \begin{cases} \lambda_i & \text{if } \lambda_i > \lambda_{\max}/\kappa_{tg} \\ \lambda_{\max}/\kappa_{tg} & \text{otherwise,} \end{cases} \quad (46)$$

where $f(\cdot)$ is the spectral function. This strategy is applied independently to rotational and translational eigenvalues with their respective parameters $\lambda_{R,\max}$, $\lambda_{t,\max}$, and κ_{tg} . This *cluster-wise constant clamping* formulation ensures that despite potential arbitrary rotations of eigenvectors within degenerate subspaces, the overall spectral modification remains consistent and basis-invariant. The clamping operates uniformly on all eigenvalues within each cluster, avoiding numerical artifacts that could arise from arbitrary eigenvector orientations (Section 5.3).

The elegance of this approach lies in its selective intervention: well-conditioned eigenvalues remain unmodified, preserving their natural convergence behavior, while ill-conditioned eigenvalues are clamped to ensure a bounded condition number. Through this targeted preconditioning, the condition number of the system is maintained within a well-defined range regardless of degeneracy severity, thereby mitigating noise amplification in weakly-constrained directions and accelerating convergence.

Crucially, the preconditioner \mathbf{P} modifies only the iterative geometry and convergence rate without altering the minimum of the original problem. Unlike global TReg, which overdamps well-conditioned directions, or TSVD, which discards weak information entirely, our eigenvalue clamping strategy performs minimal necessary spectral shaping exclusively within degenerate subspaces. As proven in Section 6.3, this approach preserves the optimal solution in observable subspaces while ensuring controlled convergence without contaminating well-conditioned directions.

6.3 Theoretical Foundation for Targeted Stabilization

We now present two complementary perspectives that justify eigenvalue clamping in the preconditioner design: an optimization perspective showing solution equivalence on observable subspace \mathcal{V} , and a probabilistic perspective interpreting selective regularization as Maximum-A-Posteriori (MAP) estimation.

Theorem 3. Equivalent Reconstruction on Decoupled Subspace. Let $\mathbf{S}_R = \mathbf{V}_R \mathbf{\Lambda}_R \mathbf{V}_R^\top$ be the eigendecomposition of the rotation Schur complement with $\mathbf{\Lambda}_R = \text{diag}(\lambda_{R,1}, \lambda_{R,2}, \lambda_{R,3})$, $0 \leq \lambda_{R,1} \leq \lambda_{R,2} \leq \lambda_{R,3}$. For the reduced quadratic:

$$Q(\phi) = \frac{1}{2} \phi^\top \mathbf{S}_R \phi - \tilde{\mathbf{g}}_R^\top \phi + \text{const} \quad (47)$$

where $\tilde{\mathbf{g}}_R = \mathbf{g}_R - \mathbf{H}_{Rt} \mathbf{H}_{tt}^{-1} \mathbf{g}_t$, the following holds:

- (i) $\tilde{\mathbf{g}}_R \in \text{range}(\mathbf{S}_R)$
- (ii) $\phi^* = \mathbf{S}_R^+ \tilde{\mathbf{g}}_R$, where $\mathbf{S}_R^+ = \mathbf{V}_R \mathbf{\Lambda}_R^+ \mathbf{V}_R^\top$
- (iii) $\forall i : \lambda_{R,i} > 0 \Rightarrow [\mathbf{V}_R^\top \phi^*]_i = \lim_{\epsilon \rightarrow 0^+} [\mathbf{V}_R^\top \phi_\epsilon]_i$

where ϕ_ϵ solves $(\mathbf{S}_R + \epsilon \mathbf{I}) \phi_\epsilon = \tilde{\mathbf{g}}_R$. Analogous results hold for the translation subproblem with \mathbf{S}_t .

Proof: See Section B.1.

Theorem 4. MAP Regularization via Eigenvalue Clamping.

Given target condition number $\kappa_{tg} > 1$, define:

$$\tilde{\lambda}_{R,i} = \max\left(\lambda_{R,i}, \frac{\lambda_{R,3}}{\kappa_{tg}}\right), \quad i \in \{1, 2, 3\} \quad (48)$$

Let $\mathbf{\Gamma}_R = \mathbf{V}_R \text{diag}(\tilde{\lambda}_{R,i} - \lambda_{R,i}) \mathbf{V}_R^\top$. Then:

- (i) The regularized problem

$$\arg \min \phi^\top \frac{1}{2} \phi^\top (\mathbf{S}_R + \mathbf{\Gamma}_R) \phi - \tilde{\mathbf{g}}_R^\top \phi \quad (49)$$

is equivalent to MAP estimation with prior $\phi \sim \mathcal{N}(\mathbf{0}, \mathbf{\Gamma}_R^{-1})$

- (ii) $\mathbf{S}_R + \mathbf{\Gamma}_R = \mathbf{V}_R \tilde{\mathbf{\Lambda}}_R \mathbf{V}_R^\top$ where $\tilde{\mathbf{\Lambda}}_R = \text{diag}(\tilde{\lambda}_{R,i})$

- (iii) $\kappa(\mathbf{S}_R + \mathbf{\Gamma}_R) \leq \kappa_{tg}$

Analogous results hold for the translation with \mathbf{S}_t .

Proof: See Section B.2.

Remark 4. These theorems establish that our preconditioner \mathbf{P} from Equation (43) with clamped eigenvalues achieves: (i) preservation of observable components, (ii) bounded condition number $\kappa(\mathbf{P}^{-1} \mathbf{H}) \leq \kappa_{tg}$, and (iii) selective regularization only on degenerate directions.

7 Experiments

7.1 Experimental Setup

7.1.1 Datasets and Experimental Scenarios We evaluate DCRreg on both simulated and real-world datasets encompassing three distinct categories for baseline comparison: (1) insufficient geometric constraints in confined environments (stairs, caves), (2) compound degeneracy (corridors, parking lot), and (3) well-constrained scenarios (building).

Simulated Dataset: Following the protocol established in Tuna et al. (2025), we employ a symmetric cylinder scenario (Figure 7) with controlled perturbations to analyze convergence behavior under certain degeneracy conditions. The perturbed point cloud is registered with the original to obtain ground truth transformations with absolute accuracy.

Real-world Datasets: Our evaluation leverages public benchmarks including FusionPortable (FP) Jiao et al. (2022); Wei et al. (2024), GEODE Chen et al. (2024b), and SubT-MRS Zhao et al. (2024b,a), supplemented by self-collected sequences (MS) captured using a Pandar XT-32 LiDAR with RTK-INS ground truth. To induce more controlled degeneracy conditions for comprehensive analysis, we artificially limit the LiDAR sensing range in some sequences (e.g., parking lot and corridor). Dataset characteristics are summarized in Table 2 and Figure 6.

7.1.2 Baseline and Evaluation Metrics We compare against state-of-the-art methods addressing ill-conditioned registration, categorized by their approach:

- **Detection methods:** ME (Minimum Eigenvalue) Zhang and Singh (2014), FCN (Full Condition Number) Hinduja et al. (2019), CN (Relative Condition Number) Hu et al. (2024b).



Figure 6. Dataset scenarios and robotic platforms. The experimental environments include: (a) open parking lot Wei et al. (2024), (b) narrow cave Zhao et al. (2024b,a), (c) confined stairway Chen et al. (2024b), (d) narrow corridor Jiao et al. (2022), and (e) indoor hallway Jiao et al. (2022).

Table 2. Degenerate Scenarios in Real-world Datasets

Scene	Degenerate		Duration (s)	Sensor	Dataset
	Trans.	Rot.			
Handheld Indoor					
Corridor	✓✓	✓	572	OS128	FP
Building			572	OS128	FP
Stairs	✓	✓	331	OS64	GEODE
Open-field Outdoor					
Parking Lot	✓✓	✓	502	Pandar32	MS
Handheld					
Cave01	✓	✓	838	VLP16	SubT-MRS
Cave02	✓	✓	986	VLP16	SubT-MRS
Cave04	✓	✓	959	VLP16	SubT-MRS

Note: ✓ = degenerate dimension. Number of checkmarks indicates severity (e.g., ✓✓✓ = all 3 translation axes degenerate).

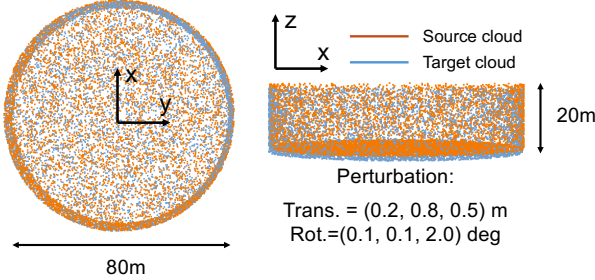


Figure 7. Symmetric cylinder scene for simulated experiments. (Left) Top-down view and (Right) side view of the cylindrical point cloud containing 7600 points. Self-registration is performed with a small perturbation consisting of a fixed rotation around the Z -axis and a large translation along Z , creating a scenario with multi-DOF degeneracy.

- **Mitigation strategies:** SR (Solution Remapping) Zhang and Singh (2014), TReg (Tikhonov Regularization) Tuna et al. (2025), TSVD (Truncated SVD) Tuna et al. (2025)
- **Complete solutions:** ME-SR Zhang and Singh (2014), FCN-SR Hinduja et al. (2019), ME-TSVD Tuna et al. (2025), ME-TReg Tuna et al. (2025), X-ICP Tuna et al. (2023), O3D Zhou et al. (2018).

For evaluation, we employ Absolute Trajectory Error (ATE) Grupp (2017) for localization accuracy, Registration accuracy (AC) and Chamfer Distance (CD) Hu et al. (2025) for mapping quality, and Degeneracy Ratio (DR) to measure the detection effectiveness for the scenarios.

7.1.3 Implementation Details Most of the baseline methods are implemented within a unified point-to-plane ICP framework based on established open-source codes* with OpenMP parallelization. Since different algorithms employ varying optimization backends, XICP[†] and SuperLoc[‡] utilize Ceres, while Open3D[§] leverages its native implementation. Our DCRreg implementation, built upon Hu et al. (2024b), employs Eigen with Intel TBB for efficient parallel computation. Table 1 summarizes the technical specifications of each approach. For system-level evaluation, we integrate each registration method into a 5s sliding-window fixed-lag smoother Hu et al. (2024b); Dellaert (2012) coupled with LiDAR-inertial odometry Xu et al. (2022). Degeneracy detection and mitigation are applied at every scan-to-map registration process to comprehensively assess their impact on long-duration localization and mapping performance. We maintain consistent configuration parameters across all methods, including correspondence search radius (1.0 m) and normal estimation (5 points). All algorithms adopt consistent hyperparameters according to the work Tuna et al. (2023, 2025): a condition number threshold of $\kappa_{th} = 10$, minimum eigenvalue threshold of 120, and convergence criteria of 10^{-3} m for translation and 10^{-5} rad for rotation. For DCRreg, the target condition number is set to $\kappa_{tg} = 10$. The max iteration for ICP is set to 30 for simulated experiments and 10 for real-world experiment. The regularization weight for Treg is fixed at $\lambda = 100$. For the XICP, we set the threshold for information sufficiency to 300 and for information deficiency to 150. The maximum and minimum alignment angle limits are specified as 45° and 60° , respectively. All experiments are conducted on an Intel i7-12700K CPU with 96 GB RAM.

7.2 Controlled Simulation Analysis

We introduce a sufficiently small initial pose perturbation to induce severe degeneracy in specific translational and rotational dimensions in Figure 7.

7.2.1 Convergence Analysis and Optimization Behavior Table 3 presents comprehensive quantitative results for the cylinder scenario. The standard O3D lacks degeneracy awareness entirely. ME-SR, ME-TSVD, and ME-TReg fail

*https://github.com/laboshin1/loam_velodyne

†<https://github.com/leggedrobotics/perfectlyconstrained>

‡<https://github.com/JokerJohn/SuperOdom-M>

§<https://github.com/isl-org/Open3D>

Table 3. Performance Comparison of Registration Algorithms on Simulated Ill-Conditioned Cylinder

Methods	Error Metrics			ICP Metrics				Degeneracy Mask	
	Trans. (cm) ↓	Rot. (deg) ↓	CD (cm) ↓	RMSE (cm) ↓	Iter. (#) ↓	Fit. (%) ↑	Time (ms) ↓	Trans. (#)	Rot. (#)
O3D	–	–	–	–	30	–	46.49	–	–
ME-SR	96.19	3.66	92.30	19.73	30	2.25	19.40	111	000
ME-TSVD	2.91	0.97	34.81	14.57	30	24.85	19.81	111	000
ME-TReg	22.18	0.11	21.96	4.18	30	34.96	20.05	111	000
FCN-SR	96.24	3.76	93.12	19.58	12	2.43	29.74	111	100
SuperLoc	23.82	2.81	71.37	43.94	—	2.29	16.98	001	000
X-ICP	0.42	2.86	55.88	18.27	9	10.08	43.06	001	000
Ours	2.71	0.05	3.29	3.16	10	100	7.79	001	000

Note: Trans. = Translation Error, Rot. = Rotation Error, RMSE = ICP Residuals, Iter. = Iteration Count, Fit. = ICP Fitness. Degeneracy Mask: Binary indicators where 1/0 represent for degenerate/well-constrained direction. Best/second-best results: blue / light blue. Unavailable data shown in –.

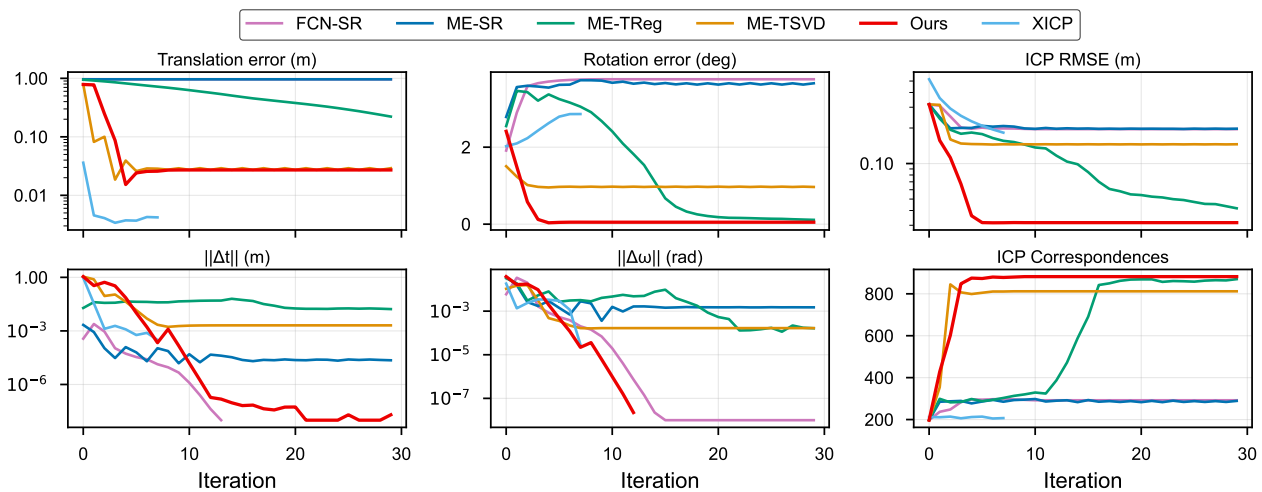


Figure 8. Iterative convergence process under cylindrical degeneracy. Plots show translation/rotation errors, update magnitudes, ICP residuals, and correspondence counts over iterations. Our method (red) exhibits faster convergence, smaller pose errors, and more stable correspondence growth than all baselines, validating its robustness in degenerate configurations.

to converge, while FCN-SR converges to a local minimum. SuperLoc exhibits substantial translation and rotation errors, indicating registration failure. Although XICP achieves the smallest translation error, its large rotation error and high Chamfer distance confirm misalignment. In contrast, our method achieves optimal performance across rotation error, Chamfer distance, ICP residual, and fitness metrics, requiring only the second-fewest iterations for successful convergence. Furthermore, our algorithm demonstrates 2 – 10 times efficient compared to baseline methods. These results validate that degeneracy detection coupled with targeted mitigation strategies effectively influences convergence and accuracy throughout the iterative process.

Regarding degeneracy detection, ME-based methods focus exclusively on absolute information while neglecting translation-rotation scale disparity, leading to over-detection in translational part. FCN-based approaches overlook coupling effects, resulting in simultaneous over-detection in both translation and rotation. More critically, the degeneracy mitigation strategy directly influences optimization trajectories during iterations. SR handle degeneracy too conservatively, TSVD discards information from multiple dimensions entirely, and TReg processes all dimensions uniformly, inadvertently introducing noise into well-conditioned dimensions. Our method uniquely achieves correct convergence.

To validate the convergence properties of our proposed method, we establish stringent convergence criteria (1×10^{-8} m for translation, 1×10^{-10} rad for rotation) to ensure sufficient iterations for comprehensive analysis of the optimization landscape. Figure 9 illustrates the optimization trajectories for z and yaw dimensions. Only our method and TReg converge to the same global minimum, with our approach requiring 16 iterations compared to TReg’s approximately 160 iterations, demonstrating superior convergence efficiency.

7.2.2 Condition Number Evolution As established in Section 4.1, the condition number directly reflects convergence speed. Figure 8 tracks the ICP behavior over iteration of different algorithms. Both translation and rotation errors decrease rapidly before stabilizing at accurate levels. Correspondingly, the update magnitudes in both rotation and translation diminish sharply, demonstrating how our optimization naturally balances the inherent scale disparity between rotational and translational parameters during the iterative process. Figure 10 compares the condition number evolution across different algorithms during iterations, alongside the relationship between subspace and full Hessian condition numbers for *DCReg*. The results demonstrate that: 1) *DCReg* achieves rapid condition number reduction

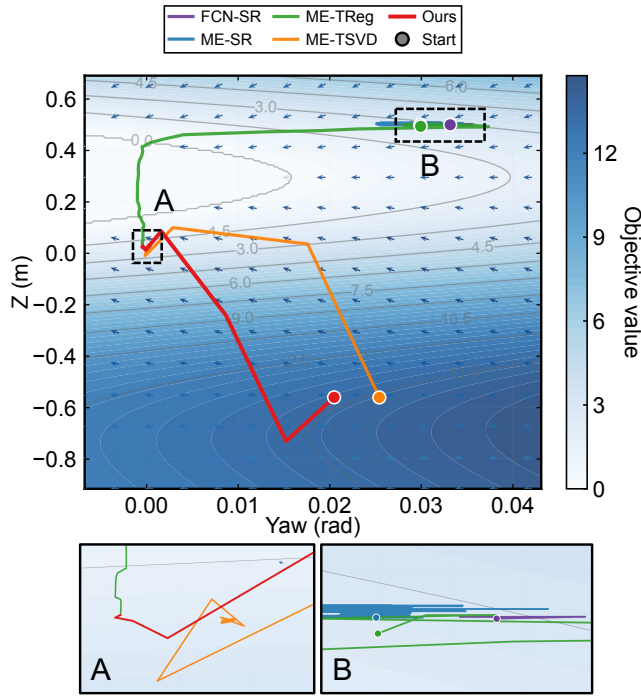


Figure 9. Optimization landscape with gradient field visualization in the cylinder scenario after 5000 iterations. Arrows indicate negative gradient directions, with optimization trajectories overlaid. Our method demonstrates the most rapid convergence.

compared to other methods, enabling faster convergence; 2) The Schur complement and full Hessian condition numbers exhibit nearly identical trends, confirming that controlling subspace conditioning directly influences the full Hessian space and optimization direction. The translational Schur complement condition number rapidly decreases to our target value $\kappa_{tg} = 10$ after degeneracy mitigation, validating the effectiveness of our mitigation strategy.

7.3 Real-world Performance Evaluation

We present comprehensive evaluation results comparing *DCReg* against baseline across diverse real-world scenarios.

7.3.1 Long-duration Localization Performance **Localization:** Table 5 presents results from challenging cave environments (indoor) characterized by extractable features but constrained passages using 16-beam LiDAR. These scenarios are particularly susceptible to constraint imbalance degeneracy when initial poses deviate or registration not converge. The cave02 involve aggressive motion patterns where most baseline methods fail entirely, yet *DCReg* achieves optimal localization accuracy. The parking lot scenario provides sufficient information but we limit the LiDAR scanning range to 10 m, yet ME fail to detect degeneracy, highlighting fundamental limitations in eigenvalue-based detection. This approach systematically overlooks rotational degeneracies due to scale disparity, as rotational eigenvalues typically maintain higher magnitudes than translational counterparts (Section 3.3).

Mapping: Table 4 extends the evaluation to include both trajectory and mapping accuracy across additional scenarios. In the constrained stair environment, FCN’s over-detection strategy leads to matching failure, while ME’s insufficient detection yields noticeable accuracy improvements under TSVD and TReg frameworks compared to odometry-only

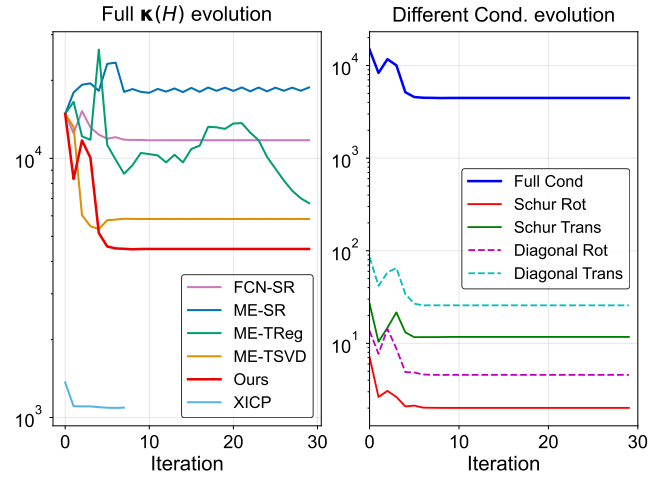


Figure 10. Condition number evolution over iteration in the cylinder degeneracy scenario. **Left:** Full Hessian condition numbers for all methods. **Right:** Schur and diagonal condition numbers for our approach.

approaches, though still inferior to *DCReg* performance. The corridor scenario reveals TReg’s inadequate regularization strength, providing minimal improvement over odometry baselines, while *DCReg* maintains optimal accuracy. In building environments, ME methods fail to detect mild degeneracies that *DCReg* successfully identifies and mitigates, resulting in measurable accuracy gains. Across all evaluated datasets, *DCReg* demonstrates substantial computational advantages, achieving 5 – 100 speedup compared to baseline approaches. This performance enhancement stems from more reliable convergence characteristics and reduced iteration requirements through targeted degeneracy mitigation.

Figure 11 visualizes mapping accuracy comparison in the stair scenario using error color map, where blue-to-red gradients indicate increasing mapping errors. *DCReg* exhibits significantly larger blue regions compared to alternative methods, corroborating the quantitative results presented in the tables and demonstrating superior spatial accuracy preservation throughout the localization process.

7.3.2 Computational Efficiency Analysis Degeneracy handling algorithms significantly impact computational performance through two primary mechanisms. First, unreliable degeneracy handling in single-frame registration can compromise initial estimates for subsequent iterations, leading to increased iteration counts and potential convergence failures. Second, in sequential SLAM applications, poor single-frame registration results propagate to affect both accuracy and efficiency of subsequent frame processing. Our computational analysis encompasses four complementary perspectives: system-level average registration times across all frames (Table 4 and Table 5), scalability analysis with varying point cloud densities (Table 6), component-wise timing breakdown (Table 7), and comparative analysis of degenerate versus non-degenerate frame processing (Table 5).

System evaluations presented in Table 4 and Table 5 demonstrate that *DCReg* achieves best computational efficiency across all datasets, realizing 5 – 100 times speedup compared to baseline. This performance gain stems from two factors: our detection and targeted mitigation strategy enables faster convergence, while the parallelized implementation optimizes computational efficiency. Table 6 illustrates the relationship between sensor range, point cloud density, and computational requirements. As LiDAR

Table 4. Comprehensive Performance Evaluation on Real-world Scenarios

Method	Stairs 3-5k pts/frame 128M pts/map				Corridor 1-2k pts/frame 67M pts/map				Building 5-10k pts/frame 241M pts/map			
	DR (%)	ATE ↓ (cm)	AC ↓ (cm)	Time ↓ (ms)	DR (%)	ATE ↓ (cm)	AC ↓ (cm)	Time ↓ (ms)	DR (%)	ATE ↓ (cm)	AC ↓ (cm)	Time ↓ (ms)
Odom	—	25.18	—	16.79	—	26.34	—	49.10	—	16.47	—	58.30
O3D	—	80.51	7.23	889.69	—	1418.37	7.09	15.02	—	16.35	5.04	377.91
ME-SR	18.91	160.75	7.90	129.19	39.27	173.82	4.55	13.31	0.00	16.53	5.72	39.37
ME-TSVD	9.26	6.44	6.09	56.16	34.84	94.32	4.36	11.60	0.00	16.56	5.74	39.16
ME-TReg	9.20	7.16	6.06	59.41	33.21	26.24	3.62	8.22	0.00	16.49	5.70	39.28
FCN-SR	94.77	280.07	7.80	207.13	85.28	231.40	6.64	38.17	17.19	337.13	6.73	685.99
Ours	50.71	3.96	5.55	6.47	58.04	7.44	3.45	1.24	15.03	13.64	5.69	4.58

Note: Best and second-best results are highlighted in blue and light blue. DR: degeneracy ratio.

Table 5. Comprehensive Performance Evaluation on Real-world Degenerate Scenarios

Method	Cave02 3-5k pts/frame 53M pts/map			Parking Lot 4-8k pts/frame 218M pts/map		
	DR (%)	ATE ↓ (cm)	Time ↓ (ms)	DR (%)	ATE ↓ (cm)	Time ↓ (ms)
Odom	—	129.78	22.39	—	32.98	22.31
O3D	—	16.88	328.53	—	36.89	345.10
ME-SR	6.47	565.61	146.80	89.59	62.11	16.01
ME-TSVD	0.83	497.05	116.54	87.69	30.46	13.96
ME-TReg	19.03	209.53	115.87	87.24	47.07	11.40
FCN-SR	58.89	491.29	232.51	98.15	64.50	17.59
Ours	32.90	4.57	3.71	86.74	29.56	2.11

Note: Best/second-best results: blue / light blue. DR: degeneracy ratio.

range increases from 10 to 60 m, point cloud size grows substantially, leading to increased degeneracy frames and correspondingly higher computational costs. This analysis validates the practical importance of efficient degeneracy handling in resource-constrained scenarios. Component-wise timing analysis in Table 7 reveals the computational costs across four key modules: degeneracy detection, mitigation, correspondence establishment, and Hessian matrix construction. Across multiple datasets, degeneracy detection and mitigation consume minimal computational resources while ensuring convergence. Correspondence establishment dominates processing time, followed by Hessian construction. Since correspondence quality directly depends on initial pose accuracy, these results underscore the critical role of reliable degeneracy handling in overall computational efficiency.

Frame-level analysis in Table 8 compares ICP iteration counts and registration times for degenerate versus non-degenerate frames across different methods. Non-degenerate frames naturally require fewer iterations and less processing time due to the absence of degeneracy issues. For degenerate frames, *DCReg* consistently achieves the lowest computational cost and competitive iteration counts. Notably, *DCReg* also demonstrates superior performance on non-degenerate frames, indicating that robust degeneracy handling in sequential processing enhances both accuracy and efficiency for subsequent registration.

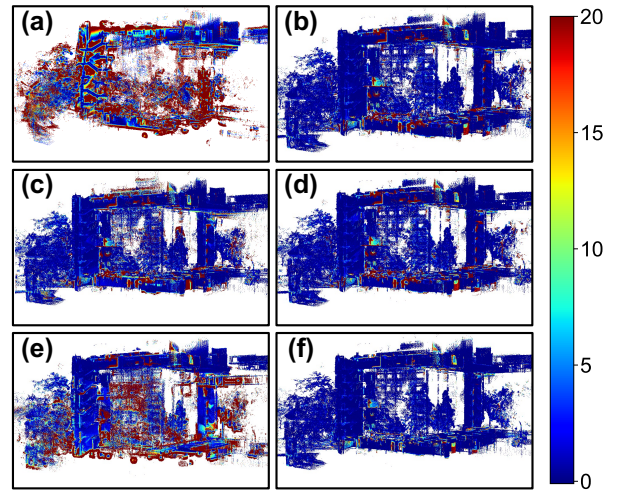


Figure 11. Map error comparison across different methods in the stairs scenario. (a):FCN-SR, (b):ME-TReg, (c):O3D, (d):ME-TSVD, (e):ME-SR, (f):Ours. The error maps use a blue-to-red scale indicating increasing error magnitude. *DCReg* exhibits predominantly blue regions compared to others, demonstrating superior mapping accuracy.

Table 6. Computational Efficiency w.r.t. Point Cloud Density

LiDAR Range (m)	Parking Lot Map: 218M pts		
	Pts. (k)	DR (%)	Time ↓ (ms)
10	1-1.5	86.74	2.11
20	2-2.5	65.0	3.40
30	3-7.5	50.29	4.35
40	4-8.5	37.00	4.96
50	5-9	33.81	5.13
60	5-10	31.08	5.99

Note: Pts. shows point count range for per-frame. DR: degeneracy ratio.

7.4 Degeneracy Analysis

7.4.1 Detection Reliability Analysis We designed comprehensive experiments to validate the effectiveness of the degeneracy detection module through three complementary analyses: dimensional degeneracy detection across different eigen dimensions over time (Figure 12), comparative analysis of *Schur complement* versus traditional diagonal condition numbers (Figure 13), and statistical comparison of specific dimensions and overall degeneracy detection rates across methods (Figure 14).

Table 7. Computational Time Breakdown of DCReg

Dataset	DR (%)	Component Time ↓				Total Time ↓
		Det.	Mit.	Corr.	Hess.	
Building	15.09	0.043	0.012	3.950	0.530	4.608
Cave01	46.53	0.043	0.011	3.460	0.380	3.910
Stairs	50.71	0.047	0.009	6.094	0.313	6.470
Parking Lot	86.74	0.064	0.071	1.662	0.212	2.105

Note: All times in ms. **DR**: degeneracy ratio, **Det.**: degeneracy detection, **Mit.**: degeneration mitigation, **Corr.**: correspondence search, **Hess.**: Hessian construction.

Figure 12 demonstrates the dimensional detection capabilities on the parking lot dataset, revealing fundamental differences in detection strategies. The FCN consistently identifies all three translational dimensions (v_0 - v_2) as degenerate throughout the process, while ME focuses primarily on the two smallest eigenvalue dimensions (v_0 , v_1). In contrast, *DCReg* simultaneously detects both translational and rotational degeneracy while correctly identifying the largest translational eigenvalue direction as non-degenerate. This behavior stems from the scale disparity problem inherent in ME and FCN approaches: translational eigenvalues consistently maintain lower magnitudes than rotational counterparts, resulting in persistently large eigenvalue ratios. Consequently, ME exhibit insufficient detection by overlooking larger eigenvalue directions, while FCN demonstrate over-detection by treating all translational dimensions as universally degenerate. Our subspace decoupling strategy effectively addresses this fundamental limitation, achieving more balanced degeneracy detection across dimensional spaces.

Figure 13 presents the condition number evolution during iterative optimization, revealing critical insights into how coupling effects between translational and rotational components impact degeneracy detection reliability. For the translational subspace, the Schur condition numbers closely align with their diagonal counterparts throughout the optimization process. This consistency can be attributed to our pose parameterization scheme ($\mathbb{R}^3 \times SO(3)$), where translation parameters maintain relative independence from rotational components in the Hessian structure. In contrast, the rotational subspace exhibits significant disparities between Schur and diagonal condition numbers, with values that can be either substantially higher or lower than diagonal estimates. This phenomenon provides empirical validation of Theorem 2, demonstrating that coupling effects fundamentally alter the conditioning characteristics of rotational components. Particularly noteworthy are regions A and B, which correspond to the planar degeneracy scenario illustrated in Figure 16. Under identical degeneracy thresholds, the Schur condition number successfully identifies the ill-conditioning, whereas the diagonal condition number incorrectly classifies the configuration as well-constrained. This discrepancy demonstrates that coupling effects can mask degeneracies when using diagonal analysis, while our Schur complement approach reliably exposes these hidden singularities.

Statistical analysis across multiple datasets in Figure 14 quantifies the detection characteristics of three methods. FCN exhibits systematic over-detection, ME demonstrates insufficient detection, while *DCReg* achieves balanced detection rates that better reflect actual degeneracy conditions.

Table 8. Convergence Performance on Degenerate vs. Non-degenerate Frames

Method	Degenerate Frames		Non-degenerate Frames	
	Iter. ↓	Time ↓ (ms)	Iter. ↓	Time ↓ (ms)
Parking Lot				
ME-SR	5.79	13.97	7.41	39.15
ME-TSVD	5.37	12.13	6.22	32.84
ME-TReg	4.63	10.05	4.17	22.13
FCN-SR	6.23	17.72	—	—
Ours	5.04	2.11	3.30	2.58
Corridor				
ME-SR	5.70	13.80	7.34	38.84
ME-TSVD	5.36	11.99	6.22	32.76
ME-TReg	4.63	10.45	4.22	22.21
Ours	4.21	2.11	3.28	1.67

Note: **DR**: degeneracy ratio. Best and second-best results are highlighted in blue and light blue. FCN-SR fails on non-degenerate frames “—”.

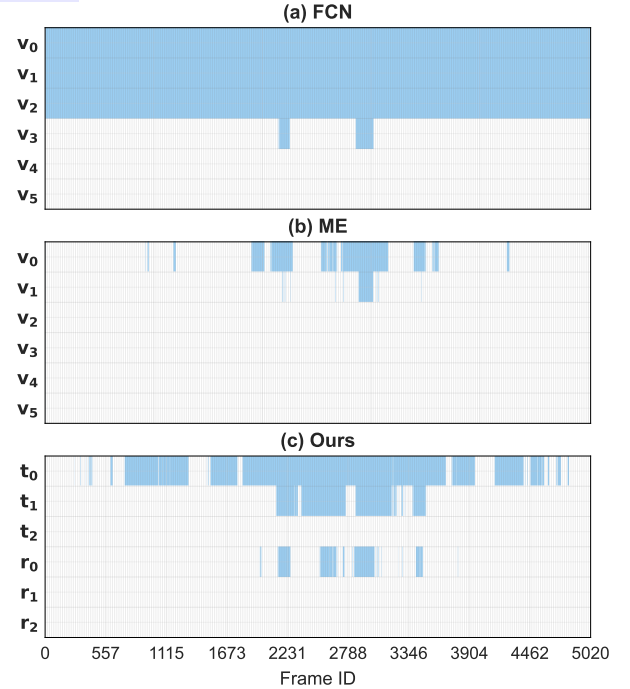


Figure 12. Temporal evolution of degeneracy detection across different directions in eigenspace on the parking lot scenario. The light blue indicating detected degeneracy. The vertical axes represent eigenvectors ordered by ascending eigenvalues.

Dimension-specific analysis reveals that all methods correctly detect the largest eigenvalue dimension (v_5) as non-degenerate, while only *DCReg* successfully detects degeneracy in the v_4 dimension, further demonstrating the enhanced reliability of our detection method.

Figure 15 examines staircase scenarios, with regions A and B corresponding to downward and upward transitions, respectively. Subplot (d) tracks the temporal evolution of condition numbers for both translational and rotational dimensions throughout the traversal. Staircase environments present unique challenges due to reduced ground plane visibility and constrained passage geometry, leading to insufficient geometric constraints and consequent degeneracy manifestations. These regions frequently exhibit coupled translational-rotational degeneracies rather than isolated single-axis singularities, indicating that geometric structure,

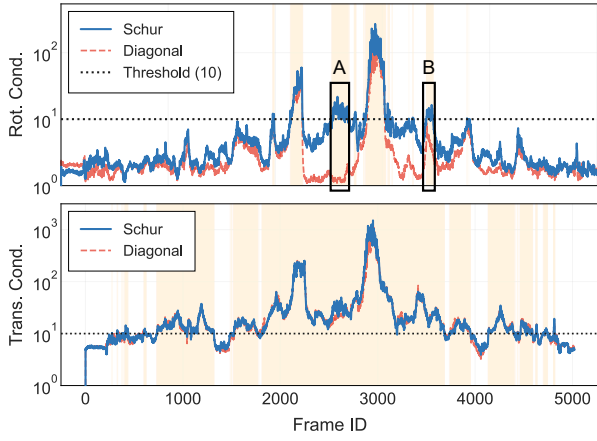


Figure 13. Condition number comparison in translational (**Down**) and rotational (**Top**) subspaces over time on the parking lot dataset. Light yellow regions indicate detected degeneracy areas with detection thresholds set to 10. Regions A and B demonstrate cases where rotational degeneracy is masked by diagonal methods.

not repetitive textures-dominates the degeneracy patterns in such confined spaces. Specifically, region A predominantly exhibits Z -axis degeneracy. Conversely, region B manifests primarily roll-pitch rotational degeneracy during ascent, where the inclined geometry provides insufficient constraints. Notably, diagonal methods fail to detect these critical degeneracies, misclassify them as well-constrained cases. This systematic under-detection further validates the superiority of our Schur complement approach in revealing masked degeneracies that compromise registration reliability in structured indoor environments.

7.4.2 Degeneracy Characterization Environmental constraints constitute the primary source of degeneracy in point cloud registration, representing inherent limitations that cannot be modified. However, initial pose serves as a critical secondary factor: when initial estimates approximate ground truth poses, even severely degenerate scenarios can achieve convergence through appropriate mitigation strategies that guide optimization directions during iterative refinement. This analysis examines degeneracy quantification and motion source across three representative scenarios: open parking lot and corridor passages, providing comprehensive characterization of common degeneracy patterns.

Parking Lot Analysis: Figure 16 presents detailed analysis of two characteristic frames from open parking areas, with left panels showing point cloud registration results against black prior map points, and right panels providing corresponding degeneracy decomposition. Frame 2314 exhibits translational degeneracy in two dimensions (t_0, t_1). Through decoupled subspace analysis, we quantify that t_0 -direction degeneracy stems from 77% X -axis motion, 13.6% Y -axis contribution, and 9.4% Z -axis influence, with t_0 oriented 12.1° relative to the X -axis. This indicates that X -axis motion primarily drives t_0 -dimensional degeneracy. Frame 2924 demonstrates additional rotational degeneracy (r_0) alongside translational components (t_0, t_1), with r_0 -direction degeneracy primarily attributable to Yaw motion. The presence of curb point clouds in green Region A provides effective rotational constraints, explaining the absence of rotational degeneracy in Frame 2314. These results align with theoretical expectations in Section 4.2: parking environments

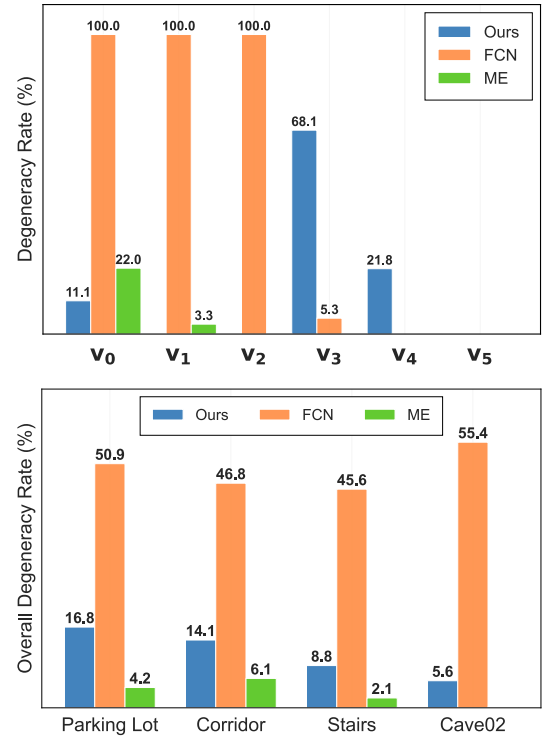


Figure 14. **Top:** degeneracy ratio comparison across different eigen directions (v_0 - v_5) for various algorithms on the parkinglot dataset. **Down:** overall degeneracy ratio comparison across different algorithms on multiple datasets.

predominantly contain ground plane points, making yaw motion constraints inherently challenging.

Corridor Analysis: Figure 17 analyzes two corridor frames under 5m LiDAR range limitation, with Regions C and D showcasing wall point clouds at corridor termini. Frame analysis reveals t_0 and r_0 degeneracies primarily driven by X -axis and roll motion components, consistent with theoretical predictions for corridor environments. In Frame 1142, increased wall points reduces degeneracy to r_0 only, validating our theoretical framework. Comparative Hessian eigenvalue analysis reveals that the smallest rotational eigenvalue actually falls below the largest translational eigenvalue, indicating that the three smallest eigenvalues in complete Hessian analysis do not necessarily correspond to translational dimensions. This phenomenon demonstrates the practical significance of eigenvalue ordering ambiguity during SVD/EVD and its impact on spectral degeneracy analysis, thereby validating the critical importance of addressing vector ambiguity issues in our *DCReg* framework.

7.5 Ablation Studies and Hybrid Analysis

7.5.1 Component Contribution Analysis The proposed *DCReg* algorithm comprises two core components: degeneracy detection and targeted PCG-based degeneracy mitigation. While the degeneracy detection module can accurately analyze dimensional degradation within subspaces and seamlessly integrate with alternative mitigation strategies, the targeted PCG mitigation method requires degeneracy detection as a prerequisite and cannot operate independently. To evaluate the contribution of each module, we conducted ablation studies on the corridor dataset with LiDAR scanning range limited to 10 m. Additionally, we examined hybrid configurations combining our detection framework with existing solvers including SR, TSVD, and TReg.

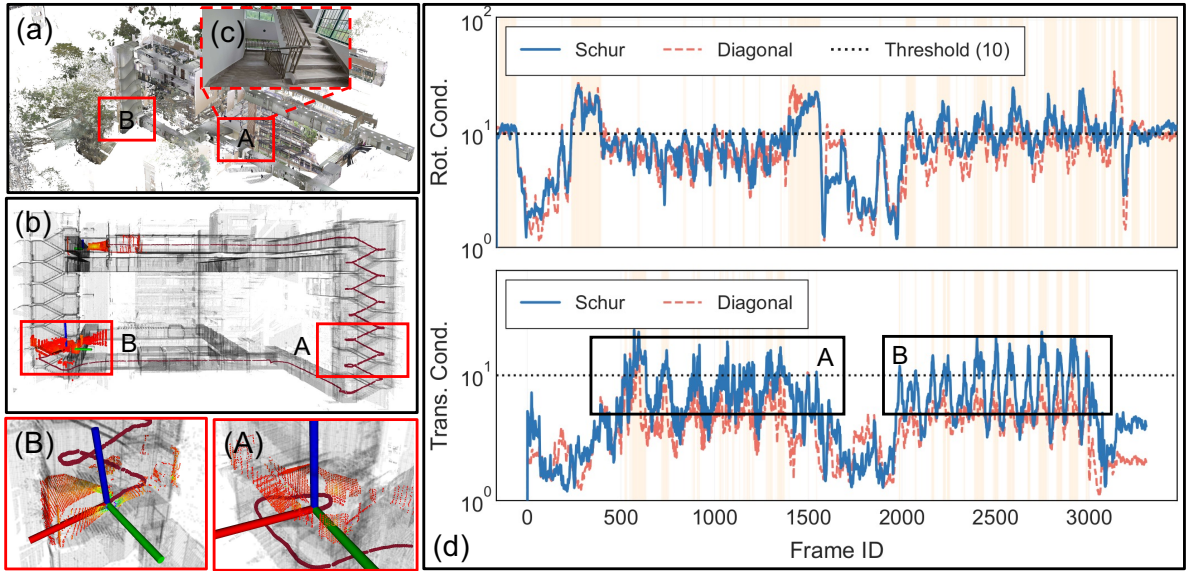


Figure 15. The figure compares two different degeneracy case caused by narrow scenarios during (A) downstairs (Z degenerate) and (B) upstairs (Roll-Pitch degenerate), with (c) showing the real-world image. (a): the ground truth point cloud map. (d): the evolution of translational and rotational condition numbers computed using our *Schur complement* versus traditional diagonal condition numbers over time. Regions A and B clearly demonstrate condition number variations corresponding to scenarios (A) and (B).

Table 9. Ablation Study and Hybrid Analysis

Corridor (DR: 58.04%)			
Configuration	ATE ↓ (cm)	AC ↓ (cm)	Time ↓ (ms)
w/o Both	28.54	3.67	1.21
w/o PCG	164.14	4.42	2.03
Hybrid Approaches (Our Detection + Traditional Mitigation)			
DCReg + SR	37.75	4.61	1.57
DCReg + TSVD	17.81	3.60	1.40
DCReg + TReg	22.79	3.51	1.89
DCReg (Full)	7.44	3.45	1.24

Note: "w/o Both" represents *DCReg* without degeneracy awareness. "w/o PCG" means no mitigation. Best and second-best results are highlighted in blue and light blue.

The comprehensive results are presented in Table 9. Without degeneracy detection or mitigation, the corridor scenario exhibited poor ATE and mapping results, albeit with minimal per-frame computational time. Interestingly, removing the PCG module while retaining detection led to degraded performance, as detected degeneracies remained unaddressed, resulting in trajectory failures and the highest overall trajectory and mapping errors.

7.5.2 Hybrid Method Evaluation For hybrid method evaluations, coupling our detection with SR-based mitigation yielded counterintuitive negative optimization for both trajectory and mapping accuracy. This degradation stems from SR's approach of discarding updates along degenerate dimensions, potentially compromising initial pose estimates for subsequent iterations and ultimately reducing registration precision. However, our detection method combined with SR significantly outperformed the baseline ME-SR approach (Table 5), validating the effectiveness of our balanced detection strategy for both translational and rotational dimensional degeneracies. Similarly, both Ours+TSVD and DCReg+TReg consistently outperformed their respective ME-TSVD and ME-TReg counterparts, further confirming

the critical importance of our degeneracy detection module. Notably, DCReg+TSVD achieved superior results compared to DCReg+TReg and Ours+SR. This performance advantage likely stems from the spectral analysis characteristics in corridor scenarios, where eigenvector ordering ambiguity (Figure 17) causes eigenvalues of degenerate rotational dimensions to approximate those of multiple translational dimensions. Under such conditions, directly discarding degenerate dimensional information may paradoxically yield better rank approximation effects. Conversely, TReg requires frequent parameter adjustments based on eigenvalue magnitudes to achieve optimal performance, which proves impractical in real-world applications. The complete *DCReg* algorithm demonstrates significant improvements in both trajectory and mapping accuracy while maintaining computational efficiency comparable to baseline methods. These results underscore that precise degeneracy detection combined with targeted mitigation substantially enhances overall registration accuracy in degenerate scenarios.

Figure 18 illustrates the ATE accuracy evolution over time for both *DCReg* and *DCReg-SR* algorithms on the parkinglot dataset. A pronounced accuracy degradation occurs in Region A, where simultaneous degeneracies in XY translation and yaw rotation manifest, resulting in substantial ATE increases. This phenomenon demonstrates the superiority of our targeted mitigation approach over conventional SR methods, as *DCReg* specifically addresses dimensional degeneracies rather than applying uniform corrections across all dimensions. The condition number analysis presented in subfigure (c) reveals two critical insights into the algorithmic behavior. First, during periods of severe degeneracy, the original problem exhibits dramatic condition number spikes, indicating numerical instability that directly correlates with the observed ATE degradation in Region A. Second, the preconditioned problem consistently maintains lower condition numbers compared to the original formulation throughout the entire trajectory, providing quantitative evidence that our PCG algorithm effectively mitigates degeneracy through systematic condition number

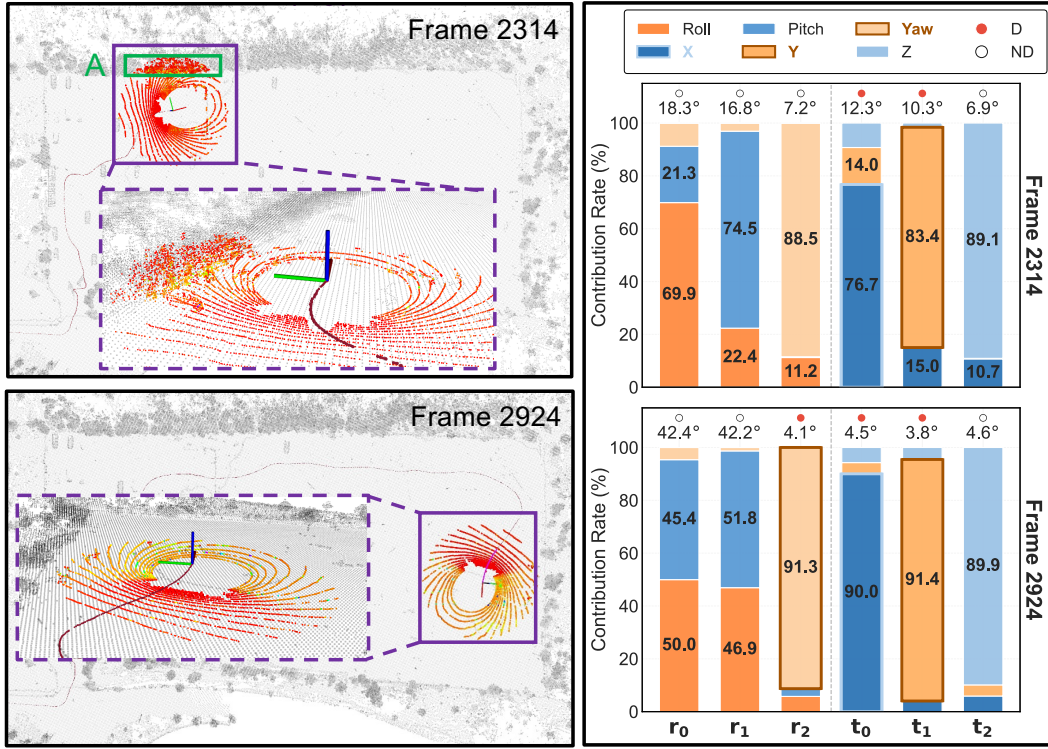


Figure 16. Planar degeneracy analysis and characterization in the parkinglot sequence. The figure illustrates degeneracy scenarios comparison between frames 2314 and 2924. In frame 2314, with the curb point clouds (region A), only X and Y degenerate. Frame 2924 contains predominantly planar point clouds, resulting in additional yaw degenerate. The right panels show the precise contribution (%) and strength (angles °) of each dimension in eigenspace ($r_0 - r_2$, $t_0 - t_2$) in terms of physical motion directions (X -yaw), enabling analysis of degeneracy motion sources.

control. This numerical conditioning improvement transform directly to the enhanced trajectory accuracy observed in the experimental results, validating the theoretical foundation of our targeted degeneracy mitigation strategy.

7.5.3 Parameter Sensitivity This section examines the sensitivity of *DCReg* to parameter variations and demonstrates the robustness of our approach compared to existing methods. The parameter analysis encompasses both the degeneracy detection and targeted mitigation modules.

For the detection module, *DCReg* requires only a single threshold parameter: the degeneracy condition number ratio. This parameter design offers significant advantages over alternative approaches. Unlike ME methods that require environment-specific parameter tuning, or FCN approaches that necessitate frequent adjustments due to scale discrepancies between translational and rotational eigenvalues, our subspace-based detection threshold possesses clear physical interpretation. The threshold is determined solely by eigenvalue ratios across different dimensions, eliminating the need for case-by-case parameter optimization. The targeted PCG module involves three parameters: the target subspace condition number κ , PCG iteration tolerance, and maximum iteration count. The latter two parameters demonstrate remarkable stability across applications. Setting the tolerance to 1×10^{-6} consistently achieves convergence within 10 iterations, rendering these parameters practically invariant across different scenarios.

Figure 19 presents a comprehensive analysis of target condition number κ_{tg} variations on the parkinglot dataset, examining trajectory accuracy, mapping precision, and average PCG iteration counts. When κ ranges from 1 to 10, both ATE and mapping accuracy remain remarkably stable while average PCG iterations increase gradually. This

behavior validates our theoretical analysis in Section 6.3, confirming that smaller condition numbers accelerate convergence and that subspace condition number control effectively influences overall optimization performance. Theoretical analysis in Section 6.3 establishes that the optimal target condition number should satisfy $1 < \kappa < 10$. Values exceeding this range can induce information loss in mildly degenerate scenarios. This prediction is also empirically confirmed in Figure 19, where configurations with $\kappa \in \{20, 50, 100\}$ exhibit significant degradation in both trajectory and mapping accuracy, validating our theoretical framework. Based on these findings, we recommend setting the κ_{tg} equal to the threshold κ_{th} in practical implementations, ensuring consistency between detection and mitigation strategies while maintaining optimal performance across diverse scenarios.

8 Discussion

This section analyzes key insights and limitations encountered in addressing degenerate registration problems, providing guidance for practical applications.

While our framework provides comprehensive analysis and solution for degenerate registration, the fundamental cause of degeneracy remains rooted in environmental geometry. In theoretically absolute degenerate scenarios, such as perfect planar surfaces or infinite corridors, certain dimensional information approaches zero, rendering any degeneracy mitigation method ineffective. However, such idealized conditions rarely exist in real-world environments. As in a near-planar surfaces, even when eigenspace dimensions exhibit insufficient information, the values remain non-zero given reasonable initial poses. Under these conditions, degeneracy mitigation methods can meaningfully improve

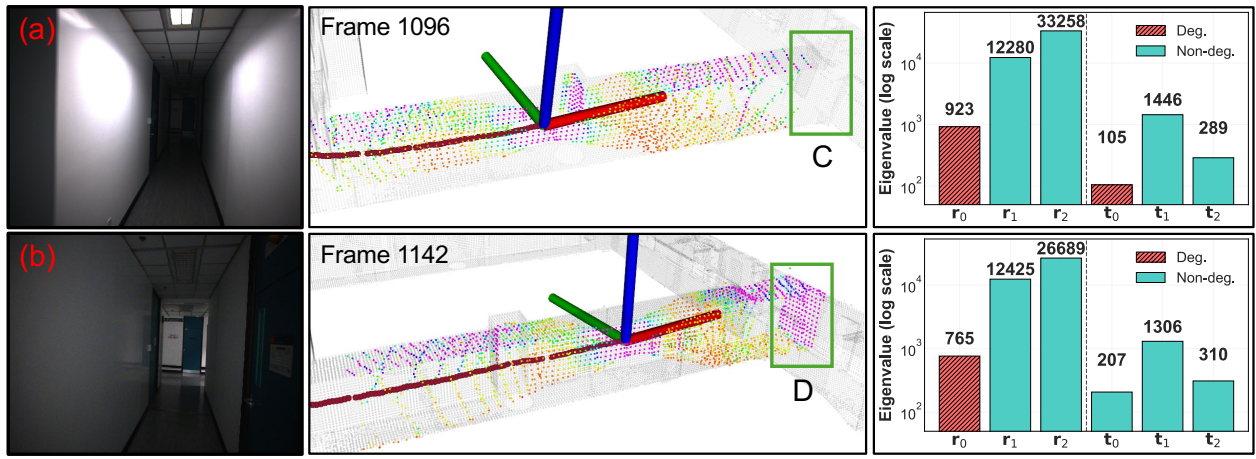


Figure 17. Eigenvector ordering ambiguity in corridor scenarios. **Left:** Real-world images at frames 1096 and 1142. **Middle:** Localization (red trajectory) and mapping results. **Right:** Eigenvalues at first ICP iteration. Frame 1096 shows X and roll degeneracy, while frame 1142 shows only roll degeneracy due to wall points in **region D**. Rotational eigenvalues are not consistently larger than translational ones, demonstrating ordering ambiguity that impacts degeneracy detection.

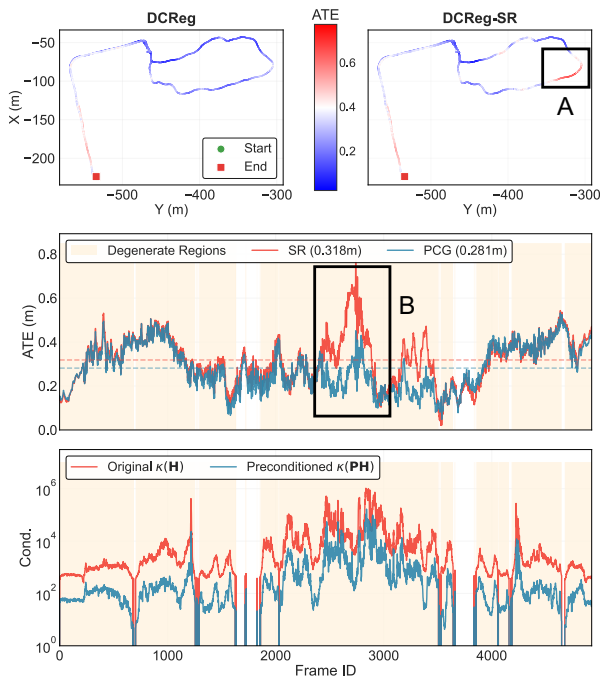


Figure 18. Trajectory error and ATE comparison over time between DCRReg and DCRReg-SR on the parkinglot dataset. DCRReg-SR exhibits significantly increased errors (Resion A and B) during trajectory segments where X Y and Yaw degenerate simultaneously, demonstrating the advantages of our targeted PCG method over SR.

numerical stability and convergence characteristics. This observation underscores the practical value of our approach in realistic scenarios where environmental geometry introduces conditioning challenges without complete information loss. The convergence basin of point cloud registration algorithms imposes a critical constraint on degeneracy mitigation effectiveness. When initial pose estimates fall outside this basin, optimization becomes trapped in local minima, rendering degeneracy analysis ineffective regardless of the mitigation strategy employed. Conversely, given reasonable initial poses within the convergence domain, degeneracy mitigation can strategically adjust pose estimation during optimization iterations, guiding the solution toward correct global optima and thereby enhancing both robustness and efficiency of registration algorithms.

This analysis reveals that reliable degenerate registration depends on the interplay between three factors: environmental

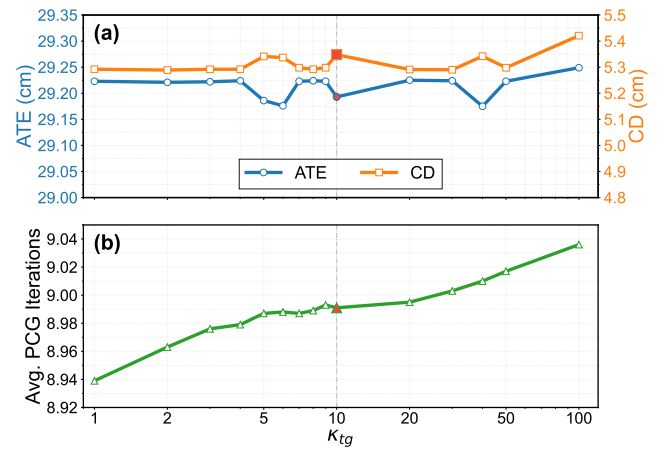


Figure 19. Parameter analysis on the parking lot dataset. (a) ATE and CD. (c) Average PCG iterations of each frame. The degeneracy detection threshold is set to 10. While PCG iterations increase monotonically with κ , both ATE and CD remain stable for $1 < \kappa < 10$, demonstrating DCRReg's robustness to parameter tuning.

geometry, initial pose, and mitigation strategy. Our framework demonstrates particular value in the intermediate regime where partial information exists and initial estimates provide reasonable starting points, conditions that characterize the majority of practical robotic applications. Understanding these boundaries helps practitioners assess when degeneracy mitigation will provide meaningful benefits and when alternative strategies may be necessary.

9 Conclusion

We present the decoupled and quantitatively characterized approach for degenerate point cloud registration with exceptional computational efficiency. Our method leverages insights from linear algebra (SVD, Schur complement, Schmidt orthogonalization), geometry (subspace analysis), estimation theory, and optimization (PCG) to design two fundamental modules: subspace decoupling and targeted-PCG solver. The subspace decoupling module employs Schur complement to eliminate rotation-translation coupling effect while quantifying relationships between eigenspace directions and physical motions. This enables reliable degeneracy detection by explaining motion induced degeneracy sources in specific environments. The targeted-PCG solver provides directional condition number enhancement for

identified degenerate directions, improving convergence and optimization stability. We provide comprehensive theoretical analysis for both modules, representing the rigorous treatment of their kind for degenerate registration problems.

Extensive validation across simulated and real-world datasets demonstrates four key advantages: (1) significant improvements in trajectory and mapping accuracy during long-duration slam tasks, (2) enhanced convergence reliability with 5 – 100 speedup in average registration performance, (3) quantitative characterization of degeneracy sources across diverse scenarios, and (4) seamless integration capability with existing degeneracy mitigation methods while achieving accuracy improvements. Our efficient open-source C++ implementation facilitates broader adoption.

Beyond core contributions, DCR_{eg} provides a fundamental analytical framework revealing that pose estimation depends entirely on correspondence pairs that evolve with initial poses during iteration. Consequently, degeneracy stems not only from repetitive geometric features (e.g., tunnels) but also from sparse environments and poor initial poses causing insufficient constraints. This insight opens numerous research opportunities for advancing LiDAR-based safe and reliable perception systems. Future work includes extending degeneracy analysis and mitigation to long-duration localization scenarios and investigating applications in multi-modal sensor fusion and dynamic environment handling. The theoretical framework established here provides a foundation for addressing ill-conditioned estimation problems across diverse robotic perception tasks.

Acknowledgements

The authors gratefully acknowledge the valuable contributions that made this work possible. We extend special thanks to Mr. Binqian Jiang and Dr. Jianhao Jiao for their insightful discussions that significantly contributed to refining the theoretical framework presented in this paper. We also appreciate Mr. Turcan Tuna for his technical assistance with the baseline algorithm implementation.

References

- Agarwal S, Mierle K and Team TCS (2023) Ceres Solver. URL <https://github.com/ceres-solver/ceres-solver>.
- Carrillo H, Latif Y, Rodriguez-Arevalo ML, Neira J and Castellanos JA (2015) On the monotonicity of optimality criteria during exploration in active slam. In: *2015 IEEE International Conference on Robotics and Automation (ICRA)*. IEEE, pp. 1476–1483.
- Chen Z, Chen H, Qi Y, Zhong S, Feng D, Wu J, Wen W and Liu M (2024a) Relead: Resilient localization with enhanced lidar odometry in adverse environments. In: *2024 IEEE International Conference on Robotics and Automation (ICRA)*. pp. 3999–4005. DOI:10.1109/ICRA57147.2024.10611074.
- Chen Z et al. (2024b) Heterogeneous lidar dataset for benchmarking robust localization in diverse degenerate scenarios. *arXiv preprint arXiv:2409.04961*.
- Dellaert F (2012) Factor graphs and gtsam: A hands-on introduction. *Georgia Institute of Technology, Tech. Rep 2*: 4.
- Ebadi K, Bernreiter L, Biggie H, Catt G, Chang Y, Chatterjee A, Denniston CE, Deschênes SP, Harlow K, Khattak S et al. (2023) Present and future of slam in extreme environments: The darpa sub challenge. *IEEE Transactions on Robotics* 40: 936–959.
- Golub GH, Hansen PC and O’Leary DP (1999) Tikhonov regularization and total least squares. *SIAM journal on matrix analysis and applications* 21(1): 185–194.
- Golub GH and Van Loan CF (2013) *Matrix computations*. JHU press.
- Grupp M (2017) evo: Python package for the evaluation of odometry and slam. <https://github.com/MichaelGrupp/evo>.
- Hansen PC (1990) Truncated singular value decomposition solutions to discrete ill-posed problems with ill-determined numerical rank. *SIAM Journal on Scientific and Statistical Computing* 11(3): 503–518.
- Hatleskog J and Alexis K (2024) Probabilistic degeneracy detection for point-to-plane error minimization. *IEEE Robotics and Automation Letters* 9(12): 11234–11241. DOI:10.1109/LRA.2024.3484153.
- He D, Xu W, Chen N, Kong F, Yuan C and Zhang F (2023) Pointlio: Robust high-bandwidth light detection and ranging inertial odometry. *Advanced Intelligent Systems* 5(7): 2200459.
- Hinduja A, Ho BJ and Kaess M (2019) Degeneracy-aware factors with applications to underwater slam. In: *2019 IEEE/RSJ International Conference on Intelligent Robots and Systems (IROS)*. IEEE, pp. 1293–1299.
- Horn RA and Johnson CR (2013) *Matrix Analysis*. 2 edition. Cambridge University Press.
- Hu X, Wu J, Jia M, Yan H, Jiang Y, Jiang B, Zhang W, He W and Tan P (2025) Mapeval: Towards unified, robust and efficient slam map evaluation framework. DOI:10.1109/LRA.2025.3548441.
- Hu X et al. (2024a) Ms-mapping: An uncertainty-aware large-scale multi-session lidar mapping system. *preprint arXiv:2408.03723*.
- Hu X et al. (2024b) Paloc: Advancing slam benchmarking with prior-assisted 6-dof trajectory generation and uncertainty estimation. *IEEE/ASME Transactions on Mechatronics* 29(6): 4297–4308. DOI:10.1109/TMECH.2024.3362902.
- Huang H et al. (2021) On bundle adjustment for multiview point cloud registration. *IEEE Robotics and Automation Letters* 6(4): 8269–8276.
- Jiao J, Zhu Y, Ye H, Huang H, Yun P, Jiang L, Wang L and Liu M (2021a) Greedy-based feature selection for efficient lidar slam. In: *2021 IEEE international conference on robotics and automation (ICRA)*. IEEE, pp. 5222–5228.
- Jiao J et al. (2021b) Robust odometry and mapping for multi-lidar systems with online extrinsic calibration. *IEEE Transactions on Robotics* 38(1): 351–371.
- Jiao J et al. (2022) Fusionportable: A multi-sensor campus-scene dataset for evaluation of localization and mapping accuracy on diverse platforms. In: *2022 IEEE/RSJ International Conference on Intelligent Robots and Systems (IROS)*. IEEE, pp. 3851–3856.
- Khattak S, Nguyen H, Mascari F, Dang T and Alexis K (2020) Complementary multi-modal sensor fusion for resilient robot pose estimation in subterranean environments. In: *2020 International Conference on Unmanned Aircraft Systems (ICUAS)*. IEEE, pp. 1024–1029.
- Liu Y, Wang J and Huang Y (2021) A localizability estimation method for mobile robots based on 3d point cloud feature. In: *2021 IEEE International Conference on Real-time Computing*

- and Robotics (RCAR). IEEE, pp. 1035–1041.
- Nashed SB, Park JJ, Webster R and Durham JW (2021) Robust rank deficient slam. In: *2021 IEEE/RSJ International Conference on Intelligent Robots and Systems (IROS)*. IEEE, pp. 6603–6608.
- Nobili S, Tinchev G and Fallon M (2018) Predicting alignment risk to prevent localization failure. In: *2018 IEEE International Conference on Robotics and Automation (ICRA)*. IEEE, pp. 1003–1010.
- Nubert J, Walther E, Khattak S and Hutter M (2022) Learning-based localizability estimation for robust lidar localization. In: *2022 IEEE/RSJ International Conference on Intelligent Robots and Systems (IROS)*. IEEE, pp. 17–24.
- Pomerleau F, Colas F, Siegwart R et al. (2015) A review of point cloud registration algorithms for mobile robotics. *Foundations and Trends® in Robotics* 4(1): 1–104.
- Qin C, Ye H, Pranata CE, Han J, Zhang S and Liu M (2020) Lins: A lidar-inertial state estimator for robust and efficient navigation. In: *2020 IEEE international conference on robotics and automation (ICRA)*. IEEE, pp. 8899–8906.
- Rong Z and Michael N (2016) Detection and prediction of near-term state estimation degradation via online nonlinear observability analysis. In: *2016 IEEE International Symposium on Safety, Security, and Rescue Robotics (SSRR)*. IEEE, pp. 28–33.
- Shan T et al. (2020) Lio-sam: Tightly-coupled lidar inertial odometry via smoothing and mapping. In: *2020 IEEE/RSJ international conference on intelligent robots and systems (IROS)*. IEEE, pp. 5135–5142.
- Tagliabue A, Tordesillas J, Cai X, Santamaria-Navarro A, How JP, Carlone L and Agha-mohammadi Aa (2021) Lion: Lidar-inertial observability-aware navigator for vision-denied environments. In: *Experimental robotics: The 17th international symposium*. Springer, pp. 380–390.
- Tuna T, Nubert J, Nava Y, Khattak S and Hutter M (2023) X-icp: Localizability-aware lidar registration for robust localization in extreme environments. *IEEE Transactions on Robotics* 40: 452–471.
- Tuna T, Nubert J, Pfreundschuh P, Cadena C, Khattak S and Hutter M (2025) Informed, constrained, aligned: A field analysis on degeneracy-aware point cloud registration in the wild. *IEEE Transactions on Field Robotics* : 1–1.
- Vizzo I, Guadagnino T, Mersch B, Wiesmann L, Behley J and Stachniss C (2023) Kiss-icp: In defense of point-to-point icp—simple, accurate, and robust registration if done the right way. *IEEE Robotics and Automation Letters* 8(2): 1029–1036.
- Wei H et al. (2024) Fusionportablev2: A unified multi-sensor dataset for generalized slam across diverse platforms and scalable environments. *The International Journal of Robotics Research* DOI:10.1177/02783649241303525.
- Weyl H (1912) Das asymptotische verteilungsgesetz der eigenwerte linearer partieller differentialgleichungen (mit einer anwendung auf die theorie der hohlraumstrahlung). *Mathematische Annalen* 71(4): 441–479.
- Wu J, Liu M, Zhu Y, Zou Z, Dai MZ, Zhang C, Jiang Y and Li C (2021) Globally optimal symbolic hand-eye calibration. *IEEE/ASME Transactions on Mechatronics* 26(3): 1369–1379. DOI:10.1109/TMECH.2020.3019306.
- Wu J, Sun Y, Wang M and Liu M (2019) Hand-eye calibration: 4-d procrustes analysis approach. *IEEE Transactions on Instrumentation and Measurement* 69(6): 2966–2981.
- Wu J, Zheng Y, Gao Z, Jiang Y, Hu X, Zhu Y, Jiao J and Liu M (2022) Quadratic pose estimation problems: Globally optimal solutions, solvability/observability analysis, and uncertainty description. *IEEE Transactions on Robotics* 38(5): 3314–3335.
- Xu W et al. (2022) Fast-lid2: Fast direct lidar-inertial odometry. *IEEE Transactions on Robotics* 38(4): 2053–2073.
- Xue B, Zhu Y, Liu T, Wu J, Jiao J, Jiang Y, Zhang C, Jiang X and He Z (2025) sqep: Global optimal solutions to scaled quadratic pose estimation problems. *IEEE Transactions on Instrumentation and Measurement* .
- Yang H, Shi J and Carlone L (2020) Teaser: Fast and certifiable point cloud registration. *IEEE Transactions on Robotics* 37(2): 314–333.
- Ye H, Chen Y and Liu M (2019) Tightly coupled 3d lidar inertial odometry and mapping. In: *2019 international conference on robotics and automation (ICRA)*. IEEE, pp. 3144–3150.
- Zhang J and Singh S (2014) Loam: Lidar odometry and mapping in real-time. In: *Robotics: Science and systems*, volume 2. pp. 1–9.
- Zhang J et al. (2016) On degeneracy of optimization-based state estimation problems : 809–816 DOI:10.1109/ICRA.2016.7487211.
- Zhao S, Gao Y, Wu T, Singh D, Jiang R, Sun H, Sarawata M, Qiu Y, Whittaker W, Higgins I et al. (2024a) Subt-mrs dataset: Pushing slam towards all-weather environments. In: *Proceedings of the IEEE/CVF Conference on Computer Vision and Pattern Recognition*. pp. 22647–22657.
- Zhao S, Zhu H, Gao Y, Kim B, Qiu Y, Johnson AM and Scherer S (2024b) Superloc: The key to robust lidar-inertial localization lies in predicting alignment risks. *arXiv preprint arXiv:2412.02901* .
- Zhou QY et al. (2018) Open3D: A modern library for 3D data processing. *arXiv:1801.09847* .

A Proofs for Schur-Complement Conditioning

A.1 Proof of Theorem 1

Consider the quadratic objective from the linearized system:

$$Q(\xi) = \frac{1}{2} \xi^\top H \xi + g^\top \xi \quad (50)$$

where $\xi = [\phi^\top, \delta t^\top]^\top \in \mathbb{R}^6$, $g = [g_R^\top, g_t^\top]^\top = J^\top r_0$. Expanding in block form:

$$Q(\phi, \delta t) = \frac{1}{2} \begin{bmatrix} \phi \\ \delta t \end{bmatrix}^\top \begin{bmatrix} H_{RR} & H_{Rt} \\ H_{tR} & H_{tt} \end{bmatrix} \begin{bmatrix} \phi \\ \delta t \end{bmatrix} + \begin{bmatrix} g_R \\ g_t \end{bmatrix}^\top \begin{bmatrix} \phi \\ \delta t \end{bmatrix}. \quad (51)$$

Step 1: Partial minimization. Setting $\nabla_{\delta t} Q = 0$:

$$H_{tR} \phi + H_{tt} \delta t + g_t = 0 \quad (52)$$

Solving for optimal δt given ϕ :

$$\delta t^*(\phi) = -H_{tt}^{-1} (H_{tR} \phi + g_t) \quad (53)$$

Step 2: Reduced objective. Substituting $\delta t^*(\phi)$ into Q :

$$\begin{aligned} Q_{\text{red}}(\phi) &= Q(\phi, \delta t^*(\phi)) \\ &= \frac{1}{2} \phi^\top H_{RR} \phi + \phi^\top H_{Rt} \delta t^*(\phi) \\ &\quad + \frac{1}{2} \delta t^*(\phi)^\top H_{tt} \delta t^*(\phi) + g_R^\top \phi + g_t^\top \delta t^*(\phi). \end{aligned} \quad (54)$$

After algebraic manipulation:

$$\begin{aligned} Q_{\text{red}}(\phi) &= \frac{1}{2} \phi^\top \underbrace{(H_{RR} - H_{Rt} H_{tt}^{-1} H_{tR})}_{S_R} \phi \\ &\quad + \underbrace{(g_R - H_{Rt} H_{tt}^{-1} g_t)^\top}_{\tilde{g}_R^\top} \phi + \text{const.} \end{aligned} \quad (55)$$

This establishes part (i).

Step 3: Sensitivity analysis. The reduced normal equation is:

$$S_R \phi^* = -\tilde{g}_R \quad (56)$$

Under perturbation $\tilde{g}_R \mapsto \tilde{g}_R + \Delta \tilde{g}_R$:

$$S_R(\phi^* + \Delta \phi^*) = -(\tilde{g}_R + \Delta \tilde{g}_R) \quad (57)$$

Therefore $S_R \Delta \phi^* = -\Delta \tilde{g}_R$, yielding:

$$\begin{aligned} \|\Delta \phi^*\|_2 &= \|S_R^{-1} \Delta \tilde{g}_R\|_2 \leq \|S_R^{-1}\|_2 \|\Delta \tilde{g}_R\|_2 \\ &= \lambda_{\min}^{-1}(S_R) \|\Delta \tilde{g}_R\|_2. \end{aligned} \quad (58)$$

Similarly, $\|\phi^*\|_2 = \|S_R^{-1} \tilde{g}_R\|_2 \geq \frac{\|\tilde{g}_R\|_2}{\|S_R\|_2} = \frac{\|\tilde{g}_R\|_2}{\lambda_{\max}(S_R)}$.
Combining:

$$\begin{aligned} \frac{\|\Delta \phi^*\|_2}{\|\phi^*\|_2} &\leq \frac{\lambda_{\max}(S_R)}{\lambda_{\min}(S_R)} \cdot \frac{\|\Delta \tilde{g}_R\|_2}{\|\tilde{g}_R\|_2} \\ &= \kappa(S_R) \frac{\|\Delta \tilde{g}_R\|_2}{\|\tilde{g}_R\|_2}. \end{aligned} \quad (59)$$

This proves part (ii). The proof for S_t follows by symmetry. \square

A.2 Proof of Proposition 1

Unweighted Case. Consider the Jacobian decomposition $J = [J_R \mid J_t] \in \mathbb{R}^{m \times 6}$, where $J_R \in \mathbb{R}^{m \times 3}$ and $J_t \in \mathbb{R}^{m \times 3}$ represent the rotational and translational components, respectively. The associated Hessian matrix admits the block structure:

$$H = J^\top J = \begin{bmatrix} J_R^\top J_R & J_R^\top J_t \\ J_t^\top J_R & J_t^\top J_t \end{bmatrix} = \begin{bmatrix} H_{RR} & H_{Rt} \\ H_{tR} & H_{tt} \end{bmatrix}, \quad (60)$$

where $H_{RR} = J_R^\top J_R \in \mathbb{R}^{3 \times 3}$, $H_{tt} = J_t^\top J_t \in \mathbb{R}^{3 \times 3}$, and $H_{Rt} = H_{tR}^\top = J_R^\top J_t \in \mathbb{R}^{3 \times 3}$.

The orthogonal projector onto $\text{range}(J_t)$ using the Moore-Penrose pseudoinverse is:

$$P_t = J_t J_t^+ \in \mathbb{R}^{m \times m}, \quad (61)$$

where $J_t^+ = (J_t^\top J_t)^{-1} J_t^\top$ when J_t has full column rank.

The Schur complement of H_{tt} in H yields the rotational stiffness matrix:

$$S_R = H_{RR} - H_{Rt} H_{tt}^+ H_{tR} \quad (62)$$

$$= J_R^\top J_R - J_R^\top J_t (J_t^\top J_t)^+ J_t^\top J_R \quad (63)$$

$$= J_R^\top (I_m - J_t (J_t^\top J_t)^+ J_t^\top) J_R \quad (64)$$

$$= J_R^\top (I_m - P_t) J_R. \quad (65)$$

Since P_t is an orthogonal projector (satisfying $P_t^2 = P_t$ and $P_t^\top = P_t$), the operator $(I_m - P_t)$ is the orthogonal projector onto $\text{range}(J_t)^\perp = \text{null}(J_t^\top)$. This projection removes components of $\text{range}(J_R)$ that can be explained by J_t , retaining only the rotational information that cannot be compensated by translation.

Weighted Case. Let $W \in \mathbb{R}^{m \times m}$ be a positive definite information matrix ($W \succ 0$). Define the whitened Jacobians as:

$$\tilde{J} \triangleq W^{1/2} J \in \mathbb{R}^{m \times 6}, \quad (66)$$

$$\tilde{J}_R \triangleq W^{1/2} J_R \in \mathbb{R}^{m \times 3}, \quad (67)$$

$$\tilde{J}_t \triangleq W^{1/2} J_t \in \mathbb{R}^{m \times 3}. \quad (68)$$

The weighted Hessian matrix becomes:

$$H = J^\top W J = \tilde{J}^\top \tilde{J}. \quad (69)$$

Following the same decomposition, the weighted Schur complement is:

$$S_R = J_R^\top W J_R - J_R^\top W J_t (J_t^\top W J_t)^+ J_t^\top W J_R. \quad (70)$$

Let $\tilde{P}_t = \tilde{J}_t \tilde{J}_t^+$ be the orthogonal projector onto $\text{range}(\tilde{J}_t)$ in the standard inner product. Using the identity:

$$W^{1/2} \tilde{P}_t W^{1/2} = W J_t (J_t^\top W J_t)^+ J_t^\top W, \quad (71)$$

we obtain two equivalent expressions for the weighted Schur complement:

$$S_R = J_R^\top W^{1/2} (I_m - \tilde{P}_t) W^{1/2} J_R \quad (72)$$

$$= J_R^\top [W - W J_t (J_t^\top W J_t)^+ J_t^\top W] J_R. \quad (73)$$

Define the W -orthogonal projector onto $\text{range}(J_t)$ as:

$$P_t^{(W)} \triangleq J_t (J_t^\top W J_t)^+ J_t^\top W. \quad (74)$$

This operator satisfies the properties of a W -orthogonal projector:

$$(P_t^{(W)})^2 = P_t^{(W)}, \quad (75)$$

$$(P_t^{(W)})^\top W = W P_t^{(W)}. \quad (76)$$

Therefore, the weighted rotational stiffness matrix can be expressed compactly as:

$$S_R = J_R^\top W (I_m - P_t^{(W)}) J_R, \quad (77)$$

where $(I_m - P_t^{(W)})$ is the W -orthogonal projector onto $\text{range}(J_t)^\perp$ with respect to the W -inner product $\langle u, v \rangle_W = u^\top W v$.

In both cases, the eigenvalues of S_R in the projected subspace accurately reflect the rotational information that cannot be compensated by translational degrees of freedom, providing a geometrically meaningful decomposition of the system's stiffness properties. This completes the proof. \square

A.3 Proof of Proposition 2

Under scaling $\delta t' = s\delta t$, the Hessian blocks transform as:

$$\mathbf{H}'_{tt} = s^2 \mathbf{H}_{tt}, \quad \mathbf{H}'_{Rt} = s \mathbf{H}_{Rt}, \quad \mathbf{H}'_{tR} = s \mathbf{H}_{tR} \quad (78)$$

The Schur complement are:

$$\begin{aligned} \mathbf{S}'_R &= \mathbf{H}_{RR} - \mathbf{H}'_{Rt}(\mathbf{H}'_{tt})^{-1}\mathbf{H}'_{tR} \\ &= \mathbf{H}_{RR} - (s\mathbf{H}_{Rt})(s^2\mathbf{H}_{tt})^{-1}(s\mathbf{H}_{tR}) \\ &= \mathbf{H}_{RR} - \mathbf{H}_{Rt}\mathbf{H}_{tt}^{-1}\mathbf{H}_{tR} = \mathbf{S}_R \end{aligned} \quad (79)$$

Hence $\kappa(\mathbf{S}_R)$ is invariant to translation scaling. \square

A.4 Proof of Theorem 2

Consider the Schur complement \mathbf{S}_R in Equation (18a). Since $\mathbf{H}_{tt} \succ 0$, we have $\mathbf{M}_R \succeq 0$.

Part (i): For any $\mathbf{u} \in \mathbb{R}^3$, the quadratic form:

$$\begin{aligned} \mathbf{u}^\top \mathbf{S}_R \mathbf{u} &= \arg \min_{\mathbf{v} \in \mathbb{R}^3} \left\{ \begin{bmatrix} \mathbf{u} \\ \mathbf{v} \end{bmatrix}^\top \mathbf{H} \begin{bmatrix} \mathbf{u} \\ \mathbf{v} \end{bmatrix} \right\} \\ &\leq \begin{bmatrix} \mathbf{u} \\ \mathbf{0} \end{bmatrix}^\top \mathbf{H} \begin{bmatrix} \mathbf{u} \\ \mathbf{0} \end{bmatrix} = \mathbf{u}^\top \mathbf{H}_{RR} \mathbf{u} \end{aligned} \quad (80)$$

Therefore $\mathbf{S}_R \preceq \mathbf{H}_{RR}$ in the Loewner order.

Part (ii): According to Rayleigh-Ritz Principle [Horn and Johnson \(2013\)](#), for symmetric matrices $\mathbf{A}, \mathbf{B} \in \mathbb{R}^{n \times n}$ with $\mathbf{B} \succeq 0$:

$$\lambda_i(\mathbf{A} - \mathbf{B}) \leq \lambda_i(\mathbf{A}), \quad i = 1, \dots, n. \quad (81)$$

Applying this to $\mathbf{S}_R = \mathbf{H}_{RR} - \mathbf{M}_R$ yields:

$$\lambda_i(\mathbf{S}_R) \leq \lambda_i(\mathbf{H}_{RR}), \quad i = 1, 2, 3. \quad (82)$$

Part (iii): According to Weyl's Perturbation Theorem [Weyl \(1912\)](#) For Hermitian matrices $\mathbf{A}, \mathbf{B} \in \mathbb{C}^{n \times n}$:

$$\lambda_i(\mathbf{A} + \mathbf{B}) \geq \lambda_i(\mathbf{A}) + \lambda_{\min}(\mathbf{B}), \quad i = 1, \dots, n. \quad (83)$$

Let $\mathbf{A} = \mathbf{H}_{RR}$ and $\mathbf{B} = -\mathbf{M}_R$:

$$\lambda_i(\mathbf{S}_R) \geq \lambda_i(\mathbf{H}_{RR}) - \lambda_{\max}(\mathbf{M}_R). \quad (84)$$

From the spectral radius definition and the established bounds:

$$\kappa(\mathbf{S}_R) = \frac{\lambda_{\max}(\mathbf{S}_R)}{\lambda_{\min}(\mathbf{S}_R)} \quad (85)$$

$$\leq \frac{\lambda_{\max}(\mathbf{H}_{RR})}{\lambda_{\min}(\mathbf{H}_{RR}) - \lambda_{\max}(\mathbf{M}_R)}, \quad (86)$$

where the inequality holds when $\lambda_{\min}(\mathbf{H}_{RR}) > \lambda_{\max}(\mathbf{M}_R)$. The bound for \mathbf{S}_t follows by symmetry. \square

B Proofs for Targeted Stabilization

B.1 Proof of Theorem 3

Part (i): From Proposition 1, we established that $\mathbf{S}_R = \mathbf{J}_R^\top (\mathbf{I} - \mathbf{P}_t) \mathbf{J}_R$. Following the derivation in Equation (18a), the reduced gradient after eliminating translation becomes:

$$\tilde{\mathbf{g}}_R = \mathbf{g}_R - \mathbf{H}_{Rt} \mathbf{H}_{tt}^{-1} \mathbf{g}_t = \mathbf{J}_R^\top (\mathbf{I} - \mathbf{P}_t) \mathbf{r}_0 \quad (87)$$

Since $(\mathbf{I} - \mathbf{P}_t)$ projects onto the orthogonal complement of $\text{range}(\mathbf{J}_t)$, we have $\tilde{\mathbf{g}}_R \in \text{range}(\mathbf{S}_R)$, ensuring the existence of a minimizer for $Q(\phi)$.

Part (ii): With $\tilde{\mathbf{g}}_R \in \text{range}(\mathbf{S}_R)$ established, the optimality condition $\mathbf{S}_R \phi = \tilde{\mathbf{g}}_R$ in the eigenbasis yields:

$$[\mathbf{V}_R^\top \phi]_i = \begin{cases} [\mathbf{V}_R^\top \tilde{\mathbf{g}}_R]_i / \lambda_{R,i} & \text{if } \lambda_{R,i} > 0 \\ 0 & \text{if } \lambda_{R,i} = 0 \end{cases} \quad (88)$$

This is precisely the Moore-Penrose pseudoinverse: $\phi^* = \mathbf{S}_R^+ \tilde{\mathbf{g}}_R$.

Part (iii): For the regularized system $(\mathbf{S}_R + \epsilon \mathbf{I}) \phi_\epsilon = \tilde{\mathbf{g}}_R$, following the eigenvalue analysis from Equation (12):

$$[\mathbf{V}_R^\top \phi_\epsilon]_i = \frac{[\mathbf{V}_R^\top \tilde{\mathbf{g}}_R]_i}{\lambda_{R,i} + \epsilon} \xrightarrow{\epsilon \rightarrow 0^+} [\mathbf{V}_R^\top \phi^*]_i \quad \text{for } \lambda_{R,i} > 0 \quad (89)$$

establishing invariance on observable components. \square

B.2 Proof of Theorem 4

Part (i): The MAP objective with Gaussian prior $\phi \sim \mathcal{N}(\mathbf{0}, \mathbf{\Gamma}_R^{-1})$ yields:

$$\phi_{\text{MAP}} = \arg \min_{\phi} \left[\frac{1}{2} \phi^\top \mathbf{S}_R \phi - \tilde{\mathbf{g}}_R^\top \phi + \frac{1}{2} \phi^\top \mathbf{\Gamma}_R \phi \right] \quad (90)$$

which is equivalent to the stated regularized problem with posterior Hessian $\mathbf{S}_R + \mathbf{\Gamma}_R$.

Part (ii): Using the eigenvalue clamping from Equation (46), define:

$$\mathbf{\Gamma}_R = \mathbf{V}_R \text{diag}(\tilde{\lambda}_{R,i} - \lambda_{R,i}) \mathbf{V}_R^\top \quad (91)$$

Since both \mathbf{S}_R and $\mathbf{\Gamma}_R$ share the same eigenvector basis \mathbf{V}_R :

$$\mathbf{S}_R + \mathbf{\Gamma}_R = \mathbf{V}_R \text{diag}(\lambda_{R,i} + \tilde{\lambda}_{R,i} - \lambda_{R,i}) \mathbf{V}_R^\top = \mathbf{V}_R \tilde{\mathbf{\Lambda}}_R \mathbf{V}_R^\top \quad (92)$$

Part (iii): From the clamping definition $\tilde{\lambda}_{R,i} = \max(\lambda_{R,i}, \lambda_{R,3}/\kappa_{\text{tg}})$:

- $\tilde{\lambda}_{R,3} = \lambda_{R,3}$ (maximum eigenvalue unchanged)
- $\tilde{\lambda}_{R,1} \geq \lambda_{R,3}/\kappa_{\text{tg}}$ (clamping lower bound)

Therefore: $\kappa(\mathbf{S}_R + \mathbf{\Gamma}_R) = \tilde{\lambda}_{R,3}/\tilde{\lambda}_{R,1} \leq \kappa_{\text{tg}}$. \square